Journal of The
Electrochemical Society

OPEN ACCESS

Nonlinear Electrochemical Impedance Spectroscopy for Lithium-Ion Battery Model Parameterization

To cite this article: Toby L. Kirk *et al* 2023 *J. Electrochem. Soc.* **170** 010514

Journal of The Electrochemical Society, 2023 **170** 010514

Nonlinear Electrochemical Impedance Spectroscopy for Lithium-Ion Battery Model Parameterization

Toby L. Kirk,[1,2,z] Adam Lewis-Douglas,[2,3] David Howey,[2,3] Colin P. Please,[1,2] and S. Jon Chapman[1,2]

[1]*Mathematical Institute, University of Oxford, Oxford, OX2 6GG, United Kingdom*
[2]*The Faraday Institution, Quad One, Harwell Campus, Didcot OX11 0RA, United Kingdom*
[3]*Battery Intelligence Lab, Department of Engineering Science, University of Oxford, Oxford OX1 3PJ, United Kingdom*

In this work we analyze the local nonlinear electrochemical impedance spectroscopy (NLEIS) response of a lithium-ion battery and estimate model parameters from measured NLEIS data. The analysis assumes a single-particle model including nonlinear diffusion of lithium within the electrode particles and asymmetric charge transfer kinetics at their surface. Based on this model and assuming a moderately-small excitation amplitude, we systematically derive analytical formulae for the impedances up to the second harmonic response, allowing the meaningful interpretation of each contribution in terms of physical processes and nonlinearities in the model. The implications of this for parameterization are explored, including structural identifiability analysis and parameter estimation using maximum likelihood, with both synthetic and experimentally measured impedance data. Accurate fits to impedance data are possible, however inconsistencies in the fitted diffusion timescales suggest that a nonlinear diffusion model may not be appropriate for the cells considered. Model validation is also demonstrated by predicting time-domain voltage response using the parameterized model and this is shown to have excellent agreement with measured voltage time-series data (11.1 mV RMSE).

 [DOI: 10.1149/1945-7111/acada7]

Manuscript submitted September 8, 2022; revised manuscript received November 10, 2022. Published January 13, 2023.

Supplementary material for this article is available online

Lithium-ion batteries have emerged as the dominant energy storage solution for portable electronics and electric vehicles, enabled by their high energy and power density and decreasing costs.[1] They are also increasingly of interest for renewable energy integration within the power grid. In all of these applications, battery models are used to improve understanding of performance trade-offs at design stage and for operational monitoring of key factors such as state of charge, temperature, and lifetime. Equivalent circuit models are widely used in battery management systems, but electrochemical models, such as those derived from porous electrode theory within the Doyle-Fuller-Newman (DFN) framework,[2] are also increasingly of interest for high-fidelity predictions in academia and industry.

The effectiveness of electrochemical battery models as a tool for performance understanding and improvement depends on the realism of their internal structure and parameters for the particular questions being asked. Even if measured input-output quantities such as voltage can be predicted accurately, the internal states may differ significantly from reality. This is compounded by the large number of parameters required in these models (e.g. the DFN model has more than 30 parameters) and hence values are often taken from literature, but may not apply to the specific cell at hand. Fast and noninvasive characterization techniques that can completely parameterize a physical model for a specific cell are therefore desirable.

Electrochemical impedance spectroscopy (EIS) is a widely used noninvasive frequency-domain characterization technique where a small amplitude sinusoidal current (or voltage) is applied to a device and the corresponding voltage (or current) response is measured.[3] The system response is assumed to be linear, and is traditionally fitted using "local" equivalent circuit models containing resistors, capacitors, and sometimes other ad hoc components (e.g. constant phase elements), although this may lead to overfitting and difficulties in interpretation of the underlying processes—see Ciucci et al.[4] for a review of the application of EIS to lithium-ion batteries. The assumption of a linear response in standard EIS necessarily discards information about nonlinearities that may be useful for model selection and parameterization. This information may be measured by applying a larger amplitude sinusoidal excitation to generate harmonics in the response of the device under test.

The injection of a sufficiently large amplitude sinusoidal current into a battery will result in a nonlinear voltage response, with harmonic components not only at the fundamental excitation frequency ω, but at all integer multiples of this i.e. 0, ω, 2ω, 3ω, …; see Fig. 1. The components $n\omega$ with $n \geqslant 2$ are referred to as higher harmonics, and are due entirely to nonlinearities. Several ways of analysing these harmonics have been considered,[5,6] but one approach is to assume the input amplitude is small, but larger than for linear EIS. Then a "weakly" nonlinear response is induced, with analytical predictions from the model possible via a perturbation expansion. We will refer to this technique as nonlinear EIS (NLEIS).[7] It was first widely applied in the context of solid-oxide fuel cells,[8–13] proving useful for model selection, i.e. identifying inconsistencies between proposed models and experiment. It has since been considered for many other electrochemical systems, as discussed in the review by Fasmin and Srinivasan.[14]

There has been limited application of NLEIS to lithium-ion batteries. Murbach and Schwartz,[5] using a DFN-type physical model, calculated the second and third harmonics by an expansion in current amplitude, but this required numerical solution of the spatial system of ODEs due to the model complexity. They showed that the higher harmonics are sensitive to the symmetry of the charge transfer reaction and to several parameters of interest, e.g. solid-state and electrolyte diffusivities. The authors also showed qualitative similarity between measured and predicted nonlinear impedances and that the second harmonic may be sensitive to cell ageing.[15]

There have been several other studies where moderate or large amplitude sinusoidal currents have been applied to lithium-ion batteries.[6,16–18] In particular, nonlinear frequency response analysis (NFRA) is a term used to refer to a particular type of NLEIS where there is no restriction on the input amplitude, and only the modulus (magnitude) of the harmonics is retained. No restriction on input amplitude means a stronger nonlinear response, however, the model analysis is purely numerical, with direct simulation in the time domain necessary before transformation to the frequency domain,

[z]E-mail: toby.kirk@maths.ox.ac.uk

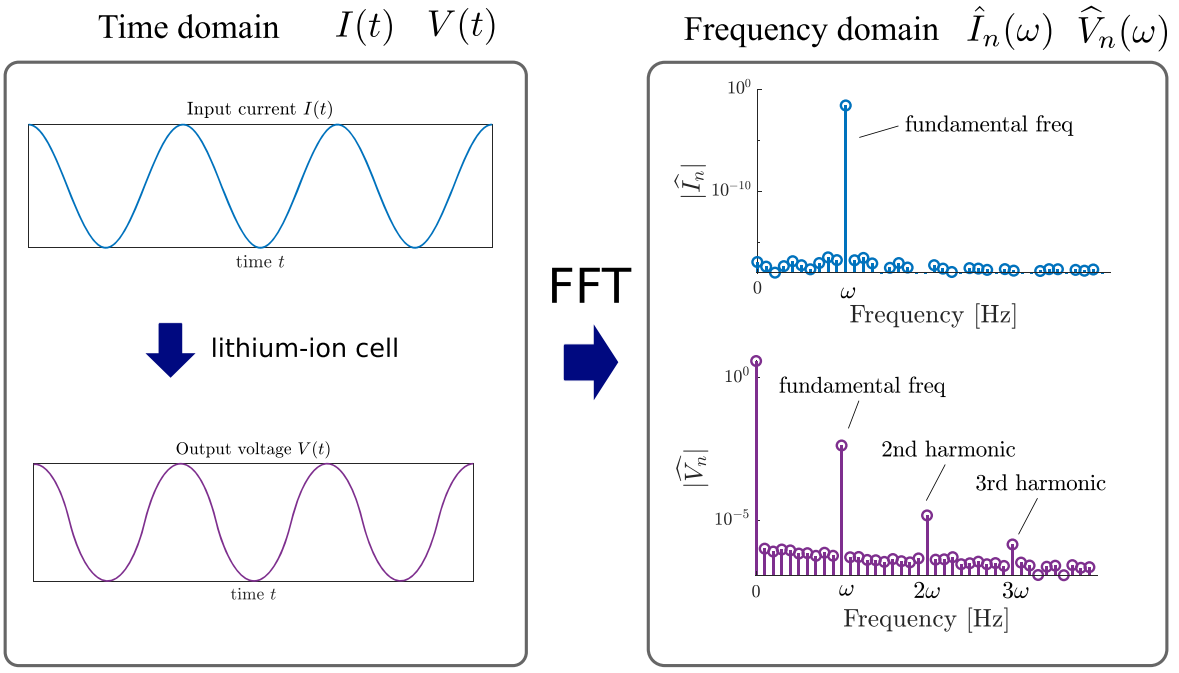

Figure 1. Diagram of the NLEIS process, where a sinusoidal current input and voltage output are transformed to the frequency domain using Fourier transforms. In practice experimental measurements are pre-processed to remove transients and windowed (e.g. with a Hann window) before transforming.

which is computationally expensive. The aforementioned "weakly nonlinear" analysis, on the other hand, can be done directly in the frequency domain. In addition, the practice in NFRA of discarding the harmonics' phase and hence potentially half of the nonlinear information does not seem justified. NFRA on lithium-ion batteries was explored experimentally by Harting et al.,[6,16] and signatures of degradation processes (e.g. lithium plating) were able to be identified. Wolff et al.[17] considered NFRA applied to a DFN-type model and performed a parameter sensitivity analysis, and they[18] investigated the signatures of several models of SEI. Large amplitude multisine signals have recently been considered by Fan et al.[19,20] who also performed a sensitivity analysis on a DFN model, giving support to the notion of asymmetry of charge transfer kinetics reported by others.[15]

Previously, NLEIS analysis of battery models has been applied only to relatively complex physical models with many parameters, such as the DFN model, making the evaluation and interpretation of the model impedances difficult. In this paper, we consider instead the NLEIS response of a reduced-order physical model, the single-particle model (SPM), which is the simplest physical model that considers each electrode separately and captures the key battery dynamics and overpotentials, e.g. Butler—Volmer reaction kinetics, solid-state diffusion of lithium, and double-layer capacitance. The SPM can also be used in modelling cell aging, e.g. chemical and mechanical degradation,[21] and is computationally simple enough to enable optimal control of grid-connected batteries.[22] Indeed, the SPM can be further simplified, e.g. to an equivalent-hydraulic model, which can in principle be deployed directly in battery management systems.[23]

The simplicity of the SPM allows us to derive analytical formulae for the impedances up to the second harmonic, and interpret each contribution in terms of physical processes, extending the established language of EIS Nyquist plots to include nonlinear harmonics. The nonlinearities are identified explicitly, originating from: (i) asymmetric Butler—Volmer kinetics; (ii) concentration dependence of the exchange current density; (iii) open circuit potential functions; (iv) solid-state diffusion. We then consider the implications of this new nonlinear information for parameter estimation, extending the structural identifiability analysis of a single-particle model by Bizeray et al.,[24] which was limited to linear impedances. This is complemented with parameter estimates from synthetic and from experimentally measured NLEIS data using a commercial pouch cell. Our results show that the model fits the impedance data

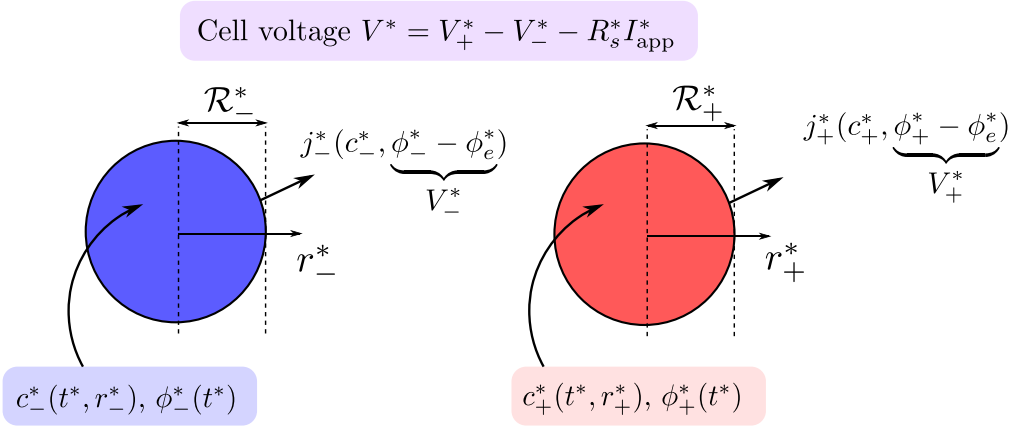

Figure 2. Single particle model schematic with a representative particle for each electrode. Not depicted is a resistor in series with the two electrodes.

accurately, capturing many of the key features of each harmonic and determining all model parameters excluding open circuit potentials. Lastly, the model is independently validated in the time domain, showing improvements in accuracy of voltage predictions over conventional methods.

Model Formulation

The single-particle model (SPM).—The model of a lithium-ion cell we consider is the single-particle model (SPM).[24–26] Here we summarise the model assumptions and governing equations. The transport of lithium ions in the electrolyte is assumed to be fast, so that they remain at a constant uniform concentration c_e^*. Throughout, asterisks denote dimensional quantities. In each electrode, the active particles that make up the porous electrode medium are all assumed identical in size and shape. Thus they behave identically, and only a model of a single representative particle is necessary. A schematic of the model geometry is shown in Fig. 2. Let the subscript $\pm$ denote that a quantity applies to, or is defined in, the positive and negative electrode, respectively. Mass transport of lithium within spherical particles of radius $\mathcal{R}_\pm^*$ is modelled here by spherically-symmetric nonlinear diffusion,

$$\frac{\partial c_\pm^*}{\partial t^*} = -\frac{1}{r_\pm^{*2}}\frac{\partial}{\partial r_\pm^*}(r_\pm^{*2} N_r^*), \qquad \text{for } 0 < r_\pm^* < \mathcal{R}_\pm^*, \tag{1}$$

$$N_r^* = -D_\pm^*(c_\pm^*)\frac{\partial c_\pm^*}{\partial r_\pm^*}, \tag{2}$$

where $c_\pm^*(r_\pm^*, t^*)$ is the concentration of lithium in the electrode material, and $D_\pm^*(c_\pm^*)$ is the nonlinear solid-state diffusion coefficient that is a function of concentration. The boundary conditions are regularity at the particle centres,

$$\frac{\partial c_\pm^*}{\partial r_\pm^*} = 0, \qquad \text{at } r_\pm^* = 0, \tag{3}$$

and a surface flux, i.e., lithium (de)intercalation into (out of) the particles,

$$-D_\pm^*(c_\pm^*)\frac{\partial c_\pm^*}{\partial r_\pm^*} = j_\pm^*, \qquad \text{at } r_\pm^* = \mathcal{R}_\pm^*, \tag{4}$$

which is modelled by nonlinear Butler—Volmer kinetics,

$$j_\pm^* = \frac{i_{0,\pm}^*(c_\pm^*)}{2F^*}\left[\exp\left(\frac{F^*(1-\beta_\pm)}{R_g^* T^*}\eta_\pm^*\right) - \exp\left(-\frac{F^*\beta_\pm}{R_g^* T^*}\eta_\pm^*\right)\right] \qquad \text{at } r_\pm^* = \mathcal{R}_\pm^*, \tag{5}$$

$$i_{0,\pm}^*(c_\pm^*) = m_\pm^*(c_\pm^*)^{\beta_\pm}(c_e^*)^{1-\beta_\pm}(c_{\pm,\max}^* - c_\pm^*)^{1-\beta_\pm}. \tag{6}$$

Here F^* is Faraday's constant, R_g^* is the universal gas constant, T^* is the temperature (assumed constant), $i_{0,\pm}^*$ is the exchange current density (with a dependence on the surface value of $c_\pm^*$, with evaluation on $r_\pm^* = \mathcal{R}_\pm^*$ assumed), $m_\pm^*$ is a reaction rate coefficient, $c_{\pm,\max}^*$ is the maximum lithium concentration in the positive/negative electrode material. The cathodic transfer coefficient $\beta_\pm$ (and corresponding anodic transfer coefficient $1-\beta_\pm$) is not assumed to be the typical value of 1/2, but may take any value between 0 and 1, i.e., $\beta_\pm \in (0,\ 1)$. Electrical conductivity in the electrode materials is assumed large, meaning the electric potential in each is uniform, only a function of time t^*, and expressed relative to the potential in the electrolyte, $V_\pm^*(t^*) = \phi_\pm^*(t^*) - \phi_e^*$. Then $\eta_\pm^*(t^*) = V_\pm^*(t^*) - U_\pm^*(c_\pm^*|_{r_\pm^*=R_\pm^*})$ is the reaction overpotential, where the open circuit potential (OCP) is given by $U_\pm^*$, a function of the surface concentration. The evaluation of $c_\pm^*$ at $r_\pm^* = \mathcal{R}_\pm^*$ in the current density and overpotential expressions will, for brevity, be understood from here on and not stated explicitly.

The nonconstant diffusion coefficient $D_\pm^*(c_\pm^*)$ will be left as a general function of $c_\pm^*$ in our analysis, but for our results we will interpret it as originating from a diffusive flux driven by chemical potential gradients, such as in concentrated solution theory. Therefore we take the radial lithium flux to be[27]

$$N_r^* = \frac{D_{\mathrm{Li},\pm}^* F^* c_\pm^*}{R_g^* T^*}\frac{\partial U_\pm^*}{\partial r_\pm^*}, \tag{7}$$

which has been shown to give more accurate behavior than a Fickian diffusion model when parameterized using galvanostatic intermittent titration technique (GITT). Here $D_{\mathrm{Li},\pm}^*$ is the constant diffusivity of the Li species in each electrode material, and the flux 7 gives rise to 1 with the concentration-dependent diffusivity

$$D_\pm^*(c_\pm^*) = -\frac{D_{\mathrm{Li},\pm}^* F^*}{R_g^* T^*}\frac{\mathrm{d}U_\pm^*}{\mathrm{d}c_\pm^*}c_\pm^*. \tag{8}$$

Note that, as per this equation, the dependence on $c_\pm^*$ is completely determined, and depends on the gradient of $U_\pm^*$.

Finally, conservation of charge relates both of the surface lithium flux densities to the macroscopic applied circuit current I_{app}^*. Let $a_\pm^*$ be the surface area per unit volume, related to the electrode volume fraction $\epsilon_\pm$ for spherical particles by $a_\pm^* = 3\epsilon_\pm/\mathcal{R}_\pm^*$, then the interfacial current density is related to the applied current via the differential equation

$$C_{\mathrm{dl},\pm}^*\frac{\mathrm{d}V_\pm^*}{\mathrm{d}t^*} = \pm\frac{I_{\mathrm{app}}^*}{\mathcal{A}^* L_\pm^* a_\pm^*} - F^* j_\pm^*, \tag{9}$$

where $I_{\mathrm{app}}^* > 0$ corresponds to a charging current, $C_{\mathrm{dl},\pm}^*$ is the double-layer capacitance at the surface of each electrode, $L_\pm^*$ is the through-cell thickness of each electrode, and $\mathcal{A}^*$ is the area of the electrodes in the transverse directions.

We include double-layer capacitance here due to its relevance in modelling the frequency domain behavior, in particular at high frequencies. However, a model neglecting double-layer capacitance has computational advantages and is particularly useful in time-domain simulations of scenarios where short timescales are less important, e.g., charging or discharging. We may neglect capacitance by setting $C_{\mathrm{dl},\pm}^* = 0$ in 9, reducing it to the algebraic equation

$$j_\pm^* = \pm\frac{I_{\mathrm{app}}^*}{F^* \mathcal{A}^* L_\pm^* a_\pm^*}. \tag{10}$$

If the applied current is prescribed, then substituting 10 into the boundary condition 4 allows 1–4 to be solved for $c_\pm^*$, and 5 subsequently inverted to give the potentials in each electrode (relative to the electrolyte potential)

$$V_\pm^* = U_\pm^*(c_\pm^*) + \eta_\pm^*. \tag{11}$$

With the potentials $V_\pm^*$ given either by the solution of 9 (when capacitance is included) or the explicit expression 11 (when capacitance is neglected), the terminal voltage for the cell is then

$$V^*(t^*) = \phi_+^* - \phi_-^* + R_s^* I_{\text{app}}^* = V_+^* - V_-^* + R_s^* I_{\text{app}}^*. \quad [12]$$

A series resistance, R_s^*, is included to account for linear resistances arising from, e.g., current collector contacts, and ionic and electronic conduction in the electrodes and electrolyte.

Scaling and nondimensional SPM.—To reduce the number of parameters required and establish the minimal set of physical parameter groups necessary to use the model, we proceed to nondimensionalise it. The internal variables $c_\pm^*$ and $r_\pm^*$ are scaled by the maximum lithium concentrations $c_{\pm,\max}^*$ and particle radii $\mathcal{R}_\pm^*$, respectively. The external variables, i.e., those directly measurable via the cell terminals such as the current I_{app}^*, voltage V^*, and time t^*, are scaled with typical values J^*, Φ^*, τ^*. It is convenient for these values to be known a priori, that is, not chosen from some internal property of the cell itself. We choose the potential scale to be the thermal voltage, $\Phi^* = F^*/(R_g^* T^*)$, and $J^* = 1$ A, $\tau^* = 1$ s.

The nondimensional variables are defined as

$$c_\pm = c_\pm^*/c_{\pm,\max}^*, \quad r = r_\pm^*/\mathcal{R}_\pm^*, \quad t = t^*/\tau^*, \quad D_\pm(c_\pm) = \frac{\tau^* D_\pm^*(c_\pm^*)}{\mathcal{R}_\pm^{*2}}, \quad [13]$$

$$I = I_{\text{app}}^*/J^*, \quad (V, V_\pm, U_\pm, \quad \eta_\pm) = (V^*, V_\pm^*, \quad U_\pm^*, \eta_\pm^*)/\Phi^*, \quad j_\pm = \frac{\tau^* j_\pm^*}{c_{\pm,\max}^* \mathcal{R}_\pm^*}, \quad [14]$$

resulting in the nondimensional model equations

$$\frac{\partial c_\pm}{\partial t} = \frac{1}{r^2}\frac{\partial}{\partial r}\left(D_\pm(c_\pm) r^2 \frac{\partial c_\pm}{\partial r}\right), \quad \text{for } 0 < r < 1, \quad [15]$$

$$\frac{\partial c_\pm}{\partial r} = 0, \text{ at } r = 0, \quad [16]$$

$$-D_\pm(c_\pm)\frac{\partial c_\pm}{\partial r_\pm} = j_\pm, \quad \text{at } r = 1, \quad [17]$$

$$c_\pm = c_{\pm,\text{init}} \quad \text{at } t = 0, \quad [18]$$

and

$$C_\pm \frac{\mathrm{d}V_\pm}{\mathrm{d}t} = \pm I(t) - \frac{j_\pm}{\xi_\pm}, \quad [19]$$

with surface fluxes, overpotentials, and terminal voltage given by

$$j_\pm = \frac{2\xi_\pm}{R_\pm(c_\pm)} E_\pm(\eta_\pm), \quad [20]$$

$$\eta_\pm = V_\pm - U_\pm(c_\pm), \quad [21]$$

$$V = V_+ - V_- + R_s I(t), \quad [22]$$

and $C_\pm$ defined later in 28. For convenience we have introduced the notation

$$E_\pm(\eta) = \frac{1}{2}[\exp((1-\beta_\pm)\eta) - \exp(-\beta_\pm \eta)], \quad [23]$$

$$R_\pm(c) = \frac{2\chi_\pm}{c^{\beta_\pm}(1-c)^{1-\beta_\pm}}, \quad [24]$$

where $\chi_\pm$ is defined below in 28. If the reactions are symmetric, i.e. $\beta_\pm = 1/2$, then $E_\pm(\eta)$ reduces to $\sinh(\eta/2)$. Here $R_\pm$ is the reciprocal of the (nondimensional) exchange current density, and can be interpreted as a nonlinear reaction resistance, with a dependence on the surface concentration $c_\pm$ (evaluation at $r_\pm = \mathcal{R}_\pm$ understood). This dependence has the nonlinear, but assumed known, functional form in 24 with parameters $\beta_\pm$ and $\chi_\pm$. The factor of 2 in 20 is necessary for $R_\pm$ to correspond to the well-known charge transfer resistance if the model is linearized—see the Nonlinear Impedance section.

If we neglect double-layer capacitance, then we may set $C_\pm = 0$ in 19, which reduces to

$$j_\pm = \pm \xi_\pm I(t), \quad [25]$$

allowing $j_\pm$ to be eliminated from the model. In this case, substituting for $j_\pm$ in 20 and rearranging for the overpotential gives

$$\eta_\pm = E_\pm^{-1}\left[\pm\frac{1}{2}R_\pm(c_\pm) I(t)\right], \quad [26]$$

where $E_\pm^{-1}$ denotes the inverse of $E_\pm$, which has no convenient closed form representation in general (note that if $\beta_\pm = 1/2$ then $E_\pm^{-1}(x) = 2\sinh^{-1}x$). The electrode potentials $V_\pm$ and terminal voltage V are then calculated from 21–22.

The remaining nondimensional parameter groups are

$$D_\pm(c_\pm) = -\frac{\tau^*}{\tau_{\text{d},\pm}^*}\frac{\mathrm{d}U_\pm}{\mathrm{d}c_\pm}c_\pm, \quad \xi_\pm = \frac{J^*\tau^*}{3Q_{\text{th},\pm}^*}, \quad \chi_\pm = \frac{R_{\text{ct,typ},\pm}^* J^*}{\Phi^*}, \quad [27]$$

$$C_\pm = \frac{C_{\text{dl},\pm}^* \Phi^* \mathcal{A}^* L_\pm^* a_\pm^*}{J^*\tau^*}, \quad R_s = \frac{R_s^* J^*}{\Phi^*}, \quad [28]$$

which are defined in terms of the following physically meaningful quantities of each electrode

$$\tau_{\text{d},\pm}^* = \frac{\mathcal{R}_\pm^{*2}}{D_{\text{Li},\pm}^*} = \text{solid state diffusion timescales} \quad [29]$$

$$R_{\text{ct,typ},\pm}^* = \frac{\Phi^*}{\mathcal{A}^* L_\pm^* a_\pm^* m_\pm^* (c_e^*)^{1-\beta_\pm} c_{\pm,\max}^*} = \text{typical charge transfer resistances} \quad [30]$$

$$Q_{\text{th},\pm}^* = F^* \epsilon_\pm c_{\pm,\max}^* L_\pm^* \mathcal{A}^* = \text{theoretical electrode capacities} \quad [31]$$

To recognize that $R_{\text{ct,typ},\pm}^*$ is an order-of-magnitude estimate of charge transfer resistance, notice that $\mathcal{A}^* L_\pm^* a_\pm^*$ is the total active surface area in each electrode, and $m_\pm^*(c_e^*)^{1-\beta_\pm} c_{\pm,\max}^*$ is the typical exchange current density, i.e. magnitude of $i_{0,\pm}^*$ from 6. Thus, the denominator in 30 is the typical reaction current.

Model parameters.—Here we summarize the model parameters necessary to use the nondimensional SPM 15–24.

OCPs and electrode balancing.—These are quantities that relate to the rest-state of the cell, and should be determined by investigations at equilibrium. They are:

- $U_\pm(c_\pm)$, the electrode OCPs (relative to a Li/Li^+ reference) as a function of stoichiometry $c_\pm \in [0, 1]$;
- $\xi_\pm$, the ratio of the theoretical electrode capacities $Q^*_{\text{th},\pm}$ to the reference scale $J^*\tau^*$;
- $c_{\pm,\text{init}}$, the initial electrode stoichiometries. These can be expressed in terms of the depth-of-discharge (DoD) of the cell, or $Q = Q^*/Q^*_{\text{cap}} \in [0, 1]$, where Q^* is the discharge capacity and Q^*_{cap} is the rated cell capacity. Then $c_{\pm,\text{init}}$ can be calculated using the linear relations

$$c_\pm = c_\pm^{0\%} + (c_\pm^{100\%} - c_\pm^{0\%})Q, \qquad [32]$$

where $c_\pm^{0\%}$ and $c_\pm^{100\%}$ are the stoichiometries at 0% and 100% DoD (i.e. $Q = 0$ and $Q = 1$). Note that these can be related to the theoretical electrode capacities, and hence $\xi_\pm$, via

$$c_\pm^{100\%} - c_\pm^{0\%} = \pm\frac{Q^*_{\text{cap}}}{Q^*_{\text{th},\pm}} = \pm\frac{3Q^*_{\text{cap}}}{J^*\tau^*}\xi_\pm, \qquad [33]$$

therefore only one of the stoichiometries in each electrode, say $c_\pm^{0\%}$, must be provided independently.In general, this amounts to requiring the knowledge of 2 functions ($U_\pm(c_\pm)$) and 4 constants ($\xi_\pm$, $c_\pm^{0\%}$) related to the balancing of the electrodes. These are typically found invasively, by disassembling a similar cell and reassembling into two half cells and then measuring the OCVs, or by the use of reference electrodes. For the experimental data used in this study, the $U_\pm$ are taken to be known as a function of DoD (or Q), measured using a minimally invasive reference electrode[24,28]—see the Methods section. We note, however, that the use of a reference electrode does not allow the electrode OCPs to be determined outside the normal operation range of the full cell. To do so, half-cell measurements would be required.

Dynamical parameters.—With the electrode balancing parameters determined, the remaining 9 parameter groups necessary for the dynamic modelling of the cell (nonzero currents) consist of 4 per electrode and 1 series resistance, as follows:

- $\tau_{\text{d},\pm} = \tau^*_{\text{d},\pm}/\tau^*$, typical diffusion timescale (scaled by the reference timescale $\tau^* = 1$ s);
- $\chi_\pm$, typical nondimensional charge transfer resistances;
- $\beta_\pm$, cathodic charge transfer coefficients;
- $C_\pm$, nondimensional double-layer capacitances;
- R_s, nondimensional series resistance.

This list of parameters can be written as a vector,

$$\boldsymbol{\theta} = (\tau_{\text{d},+}\ \chi_+\ \beta_+\ C_+\ \tau_{\text{d},-}\ \chi_-\ \beta_-\ C_-R_s)^T. \qquad [34]$$

Structural identifiability and estimation of these parameters from NLEIS data will be explored as part of the results of this paper, in the Results section.

Model nonlinearities.—Since NLEIS is a nonlinear extension of EIS, it is useful to list the various sources of nonlinearity present in the model, namely

- the OCPs, i.e. the nonlinear functions $U_\pm(c_\pm)$ which encode much of the thermodynamic behavior of the electrodes, and
- the Butler—Volmer reaction kinetics. These contribute nonlinearities in two different ways: (i) the exponential dependence of the reaction current on overpotential, given by $E_\pm(\eta_\pm)$ in 23; (ii) the dependence of the exchange current density, or equivalently the charge transfer resistance $R_\pm(c_\pm)$ in 24, on lithium concentration. Finally,
- nonlinear diffusion in the particles, i.e. the dependence of the diffusion coefficient on lithium concentration.

Each of these nonlinearities contributes to the measured nonlinear impedance, and in the following Section we will derive explicit formulae for the impedance, making each distinct contribution apparent.

Nonlinear Impedance

General description of NLEIS.—The technique of (galvanostatic) NLEIS involves the application of a sinusoidal current, $I(t; \omega, \hat{I}) = \hat{I}e^{i\omega t} + \hat{I}e^{-i\omega t} = \text{Re}\{2\hat{I}e^{i\omega t}\}$ to a device under test, where, by choice of phase, $\hat{I}$ is real and positive, giving the real representation $I = 2\hat{I}\cos\omega t$ (it is more convenient to work with $\hat{I}$, rather than the real amplitude $2\hat{I}$). Then, the nonlinear voltage response of the system, $V(t; \omega, \hat{I})$, is measured. After the decay of any initial transients, V will in general be periodic in t with period $P = 2\pi/\omega$ matching the input current, and hence have the Fourier representation

$$V(t; \omega, \hat{I}) = \sum_{n=-\infty}^{\infty} \widehat{V}_n(\omega, \hat{I})e^{in\omega t}, \quad \text{where } \widehat{V}_{-n} = \overline{\widehat{V}_n}, \qquad [35]$$

and the bar denotes complex conjugation. The component at frequency ω, matching that of the input current, is referred to as the fundamental. However, due to nonlinearities in the system, all higher harmonics, i.e. at frequencies 2ω, 3ω, …, are in general also present. The Fourier coefficients $\widehat{V}_n(\omega, \hat{I})$ depend on the excitation amplitude $\hat{I}$. Thus, we express each Fourier coefficient as a Taylor series expansion for small current amplitude $\hat{I} \ll 1$, and it can be shown[14,15] that in general,

$$\widehat{V}_n(\omega, \hat{I}) = \sum_{r=0}^{\infty} \hat{I}^{n+2r}Z_n^{(n+2r)}(\omega) = \hat{I}^n Z_n^{(n)} + \hat{I}^{n+2}Z_n^{(n+2)} + O(\hat{I}^{n+4}), \qquad [36]$$

where $Z_n^{(n+2r)}(\omega)$, n, $r = 0, 1, 2, \ldots$ are independent of $\hat{I}$. The subscript refers to the frequency mode or harmonic in the Fourier series expansion, and the superscript is the index in the Taylor series expansion in powers of $\hat{I}$. That is, a superscript (m) denotes a coefficient of $\hat{I}^m$. Then $Z_0^{(0)}$ is simply the rest (open circuit) voltage, $Z_1^{(1)}$ is the usual linear impedance, and all other $Z_n^{(n+2r)}$ with $n \geqslant 2$ or $r \geqslant 1$ are *nonlinear* impedances.

For a given harmonic n in the voltage, $\hat{I}^n Z_n^{(n)}$ is the leading-order response, and so $Z_n^{(n)}$ is the leading-order impedance for that harmonic and can be isolated from $\widehat{V}_n$ via

$$Z_n^{(n)}(\omega) = \lim_{\hat{I}\to 0}\frac{\widehat{V}_n(\omega, \hat{I})}{\hat{I}^n}. \qquad [37]$$

The higher order impedances $Z_n^{(n+2r)}$, $r \geqslant 1$, can be isolated sequentially in a similar way, provided all lower-order terms for that harmonic are first subtracted from $\widehat{V}_n$. We will focus on the leading-order impedances in this paper, e.g. $Z_1^{(1)}$ and $Z_2^{(2)}$, however $Z_0^{(2)}$ is also easily derived in this analysis.

The expansion in current amplitude $\hat{I} \ll 1$ can be performed analytically on the SPM, solving for each $Z_n^{(n+2r)}$, order-by-order, in a systematic fashion. Formally, any variable X, which includes any of the quantities $c_\pm$, $\eta_\pm$, $j_\pm$ or $V_\pm$, has a series expansion identical to 35–36. Up to $O(\hat{I}^2)$, which is the highest order we will consider here, these take the form

$$X(t;\omega,\hat{I}) = \sum_{n=-\infty}^{\infty} \widehat{X}_n(\omega,\hat{I})\mathrm{e}^{\mathrm{i}n\omega t} \quad \text{where } \widehat{X}_{-n} = \overline{\widehat{X}_n}, \qquad [38]$$

with Fourier coefficients $\widehat{X}_n$, as follows:

Zero frequency (0):

$$\hat{X}_0 = \hat{X}_0^{(0)} + \hat{I}^2\hat{X}_0^{(2)} + O(\hat{I}^4), \qquad [39]$$

Fundamental/1st harmonic (ω):

$$\hat{X}_1 = \hat{I}\hat{X}_1^{(1)} + O(\hat{I}^3), \qquad [40]$$

2nd harmonic (2ω):

$$\hat{X}_2 = \hat{I}^2\hat{X}_2^{(2)} + O(\hat{I}^4), \qquad [41]$$

Higher harmonics ($n\omega$, $n \geqslant 3$): $O(\hat{I}^3)$ [42]

SPM neglecting double-layer capacitance.—First, we consider the SPM with double-layer capacitance neglected, i.e., Eqs. 15–18, 23–26. In this case there is only a single path that the current can take through the cell, and the impedance formulae are useful in expressing the full formulae with capacitance included. We will denote the impedances without capacitance by a lowercase z to distinguish them from the full impedances with capacitance included, denoted by Z, which will be stated afterwards.

The details of the expansion are given in Section S1 of the supplementary material, and the resulting impedances for the full cell model can be written in terms of half-cell impedances $z_{n,\pm}^{(m)} = \widehat{V}_{n,\pm}^{(m)}$, found from the expansion of the half-cell voltages $V_\pm$.

At leading order in the current amplitude, there is only a zero frequency response, $z_{0,\pm}^{(0)} = U_\pm^{(0)} = U_\pm(c_\pm^{(0)})$, the OCP at the stoichiometry $c_\pm^{(0)}$ for that state of charge.

At first order, $O(\hat{I})$, there is a response at fundamental frequency given by[a]

$$z_{1,\pm}^{(1)} = \pm[R_\pm^{(0)} + Z_{1,\pm}^{\mathrm{W}}(\omega)], \qquad [43]$$

with two contributions: charge transfer resistance $R_\pm^{(0)}$ and so-called finite Warburg impedance due to the diffusion of lithium within a spherical particle,

$$Z_{1,\pm}^{\mathrm{W}}(\omega) = U_\pm^{(0)'}\frac{\xi_\pm}{D_\pm^{(0)}}H_1\left(\frac{\omega}{D_\pm^{(0)}}\right), \qquad [44]$$

where a prime denotes a derivative with respect to $c_\pm$,

$$U_\pm^{(0)'} = \left.\frac{\mathrm{d}U_\pm}{\mathrm{d}c_\pm}\right|_{c_\pm^{(0)}}, \qquad [45]$$

and a superscript (0) denotes the leading order (zero current) quantity at $c_\pm^{(0)}$. Note that $D_\pm^{(0)} = -U_\pm^{(0)'}c_\pm^{(0)}/\tau_{\mathrm{d},\pm}$, but for more generality and brevity we will leave formulae in terms of $D_\pm^{(0)}$. The function $H_1(\omega)$ encodes the frequency dependence of the transport process at this order, and is given by

$$H_1(\omega) = \frac{\tanh\sqrt{\mathrm{i}\omega}}{\tanh\sqrt{\mathrm{i}\omega} - \sqrt{\mathrm{i}\omega}}, \qquad [46]$$

with low and high ω asymptotic behaviours (differential capacitance and diffusion in a half-space, respectively)

$$H_1(\omega) \sim -\frac{3}{\mathrm{i}\omega} - \frac{1}{5}, \quad \text{as } \omega \to 0, \qquad [47]$$

$$H_1(\omega) \sim \frac{1}{1-\sqrt{\mathrm{i}\omega}} \sim -\frac{1}{\sqrt{\mathrm{i}\omega}}, \quad \text{as } \omega \to \infty\,. \qquad [48]$$

Equation 43 for the fundamental is a commonly used impedance for batteries (and many other electrochemical systems) that appears in linear EIS studies, e.g. Ref. 24.

At second order, $O(\hat{I}^2)$, there is a response at twice the excitation frequency, 2ω, found to be

$$z_{2,\pm}^{(2)} = Z_{\mathrm{asym},\pm}^{\mathrm{kin}} + Z_{\mathrm{CD},\pm}^{\mathrm{kin}} + Z_\pm^{\mathrm{OCP}} + Z_{2,\pm}^{\mathrm{W}}, \qquad [49]$$

with four contributions,

$$Z_{\mathrm{asym},\pm}^{\mathrm{kin}} = (\beta_\pm - 1/2)(R_\pm^{(0)})^2, \qquad [50]$$

$$Z_{\mathrm{CD},\pm}^{\mathrm{kin}}(\omega) = R_\pm^{(0)'}\left(\frac{\xi_\pm}{D_\pm^{(0)}}\right)H_1\left(\frac{\omega}{D_\pm^{(0)}}\right), \qquad [51]$$

$$Z_\pm^{\mathrm{OCP}}(\omega) = \frac{1}{2}U_\pm^{(0)''}\left(\frac{\xi_\pm}{D_\pm^{(0)}}\right)^2\left[H_1\left(\frac{\omega}{D_\pm^{(0)}}\right)\right]^2, \qquad [52]$$

$$Z_{2,\pm}^{\mathrm{W}}(\omega) = U_\pm^{(0)'}\left(\frac{-D_\pm^{(0)'}}{D_\pm^{(0)}}\right)\left(\frac{\xi_\pm}{D_\pm^{(0)}}\right)^2 H_2\left(\frac{\omega}{D_\pm^{(0)}}\right). \qquad [53]$$

These impedances, 50–53, each correspond to the different nonlinearities in the model, listed in the Model Formulation section. The first and second terms, 50–51, are due to nonlinearities in the kinetics. The kinetic term $Z_{\mathrm{asym},\pm}^{\mathrm{kin}}$ represents the charge transfer asymmetry, i.e. $\beta_\pm \neq 1/2$, and is purely real and independent of frequency. The kinetic term $Z_{\mathrm{CD},\pm}^{\mathrm{kin}}$ is due to the concentration dependence of the exchange current density (equivalently, the charge transfer resistance $R_\pm(c_\pm)$, see 24), which is clear from the presence of the derivative $R_\pm^{(0)'}$. The third term, $Z_\pm^{\mathrm{OCP}}$, represents the nonlinearity of the OCP with respect to stoichiometry, indicated by the second derivative appearing, $U_\pm^{(0)''}$. Finally, the term $Z_{2,\pm}^{\mathrm{W}}$ is due to nonlinear diffusion of lithium within the particles, i.e. that the diffusivity depends on concentration, indicated by $D_\pm^{(0)'}$. Therefore, it could be interpreted as a second-order finite Warburg impedance, cf. 44. Given our assumption on the functional dependence of $D_\pm^{(0)}$ (see 28), we may substitute

$$D_\pm^{(0)'} = -\frac{1}{\tau_{\mathrm{d},\pm}}(U_\pm^{(0)''}c_\pm^{(0)} + U_\pm^{(0)'}), \qquad [54]$$

into 53. At this order, the frequency dependence of the diffusion process is encoded in $H_2(\omega)$, which is the solution of a linear ODE (see Section S2 of the supplementary material), found numerically.

[a]The ± prefactor is due to the fact that a positive (charging) cell current corresponding to a charging current in the positive electrode but *discharging* current in the negative one.

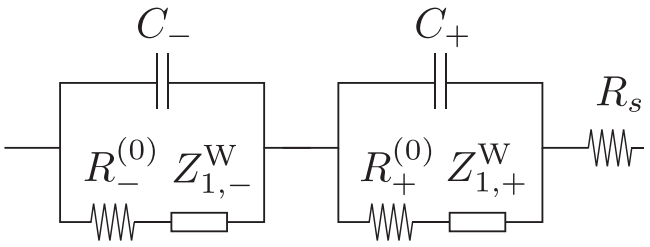

Figure 3. Equivalent circuit diagram representing the linear response of the full cell model, consisting of a Randles circuit for each electrode along with a series resistor R_s.

However, the high frequency behavior of H_2 may be extracted and is found to be

$$H_2(\omega) \sim \frac{1}{\mathrm{i}\omega}\left(1 - \frac{1}{\sqrt{2}}\right), \quad \text{as } \omega \to \infty, \tag{55}$$

which is just a real multiple of $(H_1)^2$ as $\omega \to \infty$ to leading order. If the diffusion is linear, a common simplification, then $D_\pm^{(0)'} = 0$ and the term $Z_{2,\pm}^{\mathrm{W}}(\omega)$ vanishes.

In addition to the response at 2ω, there is a nonlinear response at zero frequency, where many of the same terms arise:

$$z_{0,\pm}^{(2)} = 2\mathrm{Re}[Z_{\mathrm{asym},\pm}^{\mathrm{kin}} + Z_{\mathrm{CD},\pm}^{\mathrm{kin}} + Z_{0,\pm}^{\mathrm{OCP}} + Z_{0,\pm}^{\mathrm{W}}]. \tag{56}$$

The terms are the same as in $z_{2,\pm}^{(2)}$, 49, except for the OCP and Warburg terms, which are now

$$Z_{0,\pm}^{\mathrm{OCP}}(\omega) = \frac{1}{2}U_\pm^{(0)''}\left(\frac{\xi_\pm}{D_\pm^{(0)}}\right)^2 \left| H_1\left(\frac{\omega}{D_\pm^{(0)}}\right)\right|^2, \tag{57}$$

$$Z_{0,\pm}^{\mathrm{W}}(\omega) = U_\pm^{(0)'}\left(\frac{-D_\pm^{(0)'}}{D_\pm^{(0)}}\right)\left(\frac{\xi_\pm}{D_\pm^{(0)}}\right)^2 H_0\left(\frac{\omega}{D_\pm^{(0)}}\right), \tag{58}$$

where a different function, $H_0(\omega)$ appears in the place of $H_2(\omega)$—see Section S2 of the supplementary material. Notice that $z_{0,\pm}^{(2)}$ is real; this is because it represents a correction to the time average of the response, and hence is not oscillatory.

The nonlinear impedances at $O(\hat{I}^3)$ and higher can be readily calculated, but with diminishing returns on their usability. Their amplitude is inherently smaller, implying lower signal-to-noise ratios, with significant increase in analytical complexity, so we do not consider them here.

The impedances for the full cell, including both electrodes and a series resistance, are straightforwardly given in terms of the half-cell impedances 43, 49, 56, using 22:

$$z_0^{(0)} = z_{0,+}^{(0)} - z_{0,-}^{(0)}, \quad z_1^{(1)} = z_{1,+}^{(1)} - z_{1,-}^{(1)} + R_s, \tag{59}$$

$$z_2^{(2)} = z_{2,+}^{(2)} - z_{2,-}^{(2)}, \quad z_0^{(2)} = z_{0,+}^{(2)} - z_{0,-}^{(2)}, \tag{60}$$

Note that the series resistance R_s only enters the $z_1^{(1)}$ expression as it is assumed to be a linear resistor.

The fundamental impedance $z_1^{(1)}$ is the usual linear one, measured through conventional EIS, with dependence only on the series resistance R_s and electrode quantities $U_+^{(0)'}$, $U_-^{(0)'}$, $D_+^{(0)}$, $D_-^{(0)}$, χ_+, χ_-, β_+, β_-. The second order impedances, $z_2^{(2)}$ and $z_0^{(2)}$, additionally depend on the higher derivatives $U_+^{(0)''}$, $U_-^{(0)''}$, $D_+^{(0)'}$, $D_-^{(0)'}$. They also have explicit dependence on β_+ and β_- via the kinetic asymmetry terms $Z_{\mathrm{asym},+}^{\mathrm{kin}}$ and $Z_{\mathrm{asym},-}^{\mathrm{kin}}$.

SPM including double-layer capacitance.—We now extend the formulae of the previous Section to the more general case of the SPM that includes double-layer capacitance, 15–24. One may repeat the calculations of the previous section, starting from the full equations, but the resulting impedance formulae may be expressed concisely in terms of those already derived. The calculation of the half-cell impedances, now employing an uppercase Z to signify the inclusion of capacitance, is given in Section S1.2 of the supplementary material, and yields

$$Z_{1,\pm}^{(1)} = \frac{z_{1,\pm}^{(1)}(\omega)}{1 \pm C_\pm \mathrm{i}\omega z_{1,\pm}^{(1)}(\omega)} = \pm\left(\frac{1}{(C_\pm\mathrm{i}\omega)^{-1}} + \frac{1}{R_\pm^{(0)} + Z_{1,\pm}^{\mathrm{W}}(\omega)}\right)^{-1}, \tag{61}$$

$$Z_{2,\pm}^{(2)} = \frac{z_{2,\pm}^{(2)}(\omega)}{[1 \pm C_\pm \mathrm{i}2\omega z_{1,\pm}^{(1)}(2\omega)][1 \pm C_\pm \mathrm{i}\omega z_{1,\pm}^{(1)}(\omega)]^2}, \tag{62}$$

$$Z_{0,\pm}^{(2)} = \frac{z_{0,\pm}^{(2)}(\omega)}{|1 \pm C_\pm \mathrm{i}\omega z_{1,\pm}^{(1)}(\omega)|^2}, \tag{63}$$

where $z_{n,\pm}^{(m)}$ are the corresponding half-cell impedance formulae assuming no capacitance ($C_\pm = 0$), given by 43, 49 and 56. As there is now more than one path the current can take through each electrode, these formulae are no longer just a sum of individual impedances as in 43, 49 and 56, but they are nonetheless still explicit.

The linear impedances $Z_{1,\pm}^{(1)}$ have the clear interpretation as being the harmonic mean of $(C_\pm\mathrm{i}\omega)^{-1}$ and $z_{1,\pm}^{(1)}(\omega)$. This corresponds to a capacitor in parallel with a charge transfer resistance that is in series with a (finite) Warburg element—this is exactly the Randles circuit. The nonlinear impedances do not have such a clear analogy with traditional circuit elements. The expressions 61–63 arise from nonlinearities in the charge transfer reaction and diffusion process when they are placed in parallel with a capacitance, and therefore had to be derived mathematically rather than from physical intuition.

The impedances for a full-cell are given, using 22, by

$$Z_0^{(0)} = Z_{0,+}^{(0)} - Z_{0,-}^{(0)}, \quad Z_1^{(1)} = Z_{1,+}^{(1)} - Z_{1,-}^{(1)} + R_s, \tag{64}$$

$$Z_2^{(2)} = Z_{2,+}^{(2)} - Z_{2,-}^{(2)}, \quad Z_0^{(2)} = Z_{0,+}^{(2)} - Z_{0,-}^{(2)}. \tag{65}$$

The fundamental full-cell impedance then has the familiar equivalent circuit analogy shown in Fig. 3, consisting of two Randles circuits (one for each electrode) placed in series. We emphasise that Fig. 3 captures precisely how the impedance of the SPM is related to equivalent circuit models. The resistances and capacitances in such models are typically phenomenological and are found by fitting to data. Our analysis here shows the processes that they correspond to physically, and hence gives meaning to the resulting fitted parameter values.

Simplifications: separation of capacitance and diffusion timescales.—Although the impedance formulae 61–63 are already explicit, some further simplification is possible using common assumptions about the physical timescales in the system. There are two prominent timescales in 61–63, corresponding to capacitance and diffusion effects. These are given by $R_\pm^{(0)}C_\pm$ and $1/D_\pm^{(0)}$, respectively. Note that these timescales have been scaled by a known reference timescale τ^*. Here $1/D_\pm^{(0)} = \tau_{\mathrm{d},\pm}/(-U_\pm^{(0)'}c_\pm^{(0)})$ can be thought of as the *local* diffusion timescale, at this DoD, which is more convenient to use here instead of $\tau_{\mathrm{d},\pm}$ directly. Typically the

capacitance timescale ($O(10^{-2})$ s) is much shorter than the diffusive one ($O(10^4)$ s), hence we can consider the well-separated limit of $R_\pm^{(0)} C_\pm \ll 1/D_\pm^{(0)}$.

Taking $R_\pm^{(0)} C_\pm \ll 1/D_\pm^{(0)}$ in 61–63 gives different results depending on the frequency ω. If the frequency is sufficiently low, $\omega = O(D_\pm^{(0)})$ (region (I)), then diffusion will dominate and the effects of capacitance will be negligible, i.e. $C_\pm$ may be set to zero. If $\omega = O(D_\pm^{(0)}/(R_\pm^{(0)} C_\pm))$ (region (II)), the opposite is true and we may take the high ω limits of $z_{n,\pm}^{(m)}(\omega)$, which are real and given by

$$z_{1,\pm}^{(1)}(\omega) \to \pm R_\pm^{(0)}, \qquad \omega \to \infty, \tag{66}$$

$$z_{2,\pm}^{(2)}(\omega) \to (\beta_\pm - 1/2)(R_\pm^{(0)})^2, \qquad \omega \to \infty, \tag{67}$$

$$z_{0,\pm}^{(2)}(\omega) \to 2(\beta_\pm - 1/2)(R_\pm^{(0)})^2, \qquad \omega \to \infty. \tag{68}$$

Then approximations of 61–63 in both regions take the form

$$Z_{1,\pm}^{(1)} \sim \begin{cases} z_{1,\pm}^{(1)}(\omega) & \text{(I)}, \ \omega = O(D_\pm^{(0)}), \\ \dfrac{\pm R_\pm^{(0)}}{1 + R_\pm^{(0)} C_\pm \mathrm{i}\omega} & \text{(II)}, \ \omega = O\left(\dfrac{D_\pm^{(0)}}{R_\pm^{(0)} C_\pm}\right), \end{cases} \tag{69}$$

$$Z_{2,\pm}^{(2)} \sim \begin{cases} z_{2,\pm}^{(2)}(\omega) & \text{(I)}, \ \omega = O(D_\pm^{(0)}), \\ \dfrac{(\beta_\pm - 1/2)(R_\pm^{(0)})^2}{[1 + 2R_\pm^{(0)} C_\pm \mathrm{i}\omega][1 + R_\pm^{(0)} C_\pm \mathrm{i}\omega]^2} & \text{(II)}, \ \omega = O\left(\dfrac{D_\pm^{(0)}}{R_\pm^{(0)} C_\pm}\right), \end{cases} \tag{70}$$

$$Z_{0,\pm}^{(2)} \sim \begin{cases} z_{0,\pm}^{(2)}(\omega) & \text{(I)}, \ \omega = O(D_\pm^{(0)}), \\ \dfrac{2(\beta_\pm - 1/2)(R_\pm^{(0)})^2}{|1 + R_\pm^{(0)} C_\pm \mathrm{i}\omega|^2} & \text{(II)}, \ \omega = O\left(\dfrac{D_\pm^{(0)}}{R_\pm^{(0)} C_\pm}\right), \end{cases} \tag{71}$$

There is a narrow region between region I and region II where both capacitance and diffusive effects act with similar small strength. This narrow region occurs for frequencies

$$\omega \approx \left(\frac{-U_\pm^{(0)\prime} \xi_\pm \sqrt{D_\pm^{(0)}}}{(R_\pm^{(0)})^2 C_\pm} \right)^{2/3}. \tag{72}$$

We can now create an approximation valid for all the frequencies by forming a composite approximation made by summing the region I and II approximations and subtracting the leading order solution in the overlap region. This overlap solution is found by taking the $\omega \to \infty$ limit from region I (see 66–68) or the $\omega \to 0$ limit from region II (at the fundamental frequency, this is simply the charge transfer resistance $R_\pm^{(0)}$). The resulting composite solutions are

$$Z_{1,\pm}^{(1),\mathrm{comp}} \sim \pm \left[\frac{R_\pm^{(0)}}{1 + R_\pm^{(0)} C_\pm \mathrm{i}\omega} + Z_{1,\pm}^{\mathrm{W}}(\omega) \right], \tag{73}$$

$$Z_{2,\pm}^{(2),\mathrm{comp}} \sim \frac{Z_{\mathrm{asym},\pm}^{\mathrm{kin}}}{[1 + 2R_\pm^{(0)} C_\pm \mathrm{i}\omega][1 + R_\pm^{(0)} C_\pm \mathrm{i}\omega]^2} + Z_{\mathrm{CD},\pm}^{\mathrm{kin}} + Z_\pm^{\mathrm{OCP}} + Z_{2,\pm}^{\mathrm{W}}, \tag{74}$$

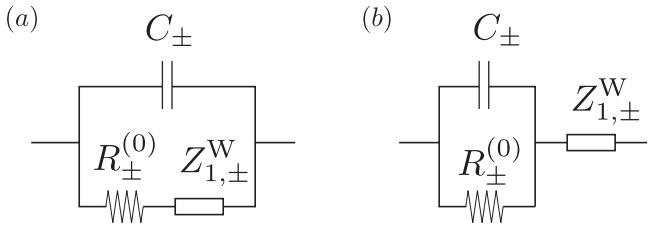

Figure 4. Equivalent circuit diagrams representing the linear response of each electrode, but corresponding to different impedance formulae. (a) Formula 61, with no assumption on the diffusion and capacitance timescales. (b) Composite (approximate) formula 73, where the timescales are assumed well-separated and the Warburg impedance acts in series with the kinetics.

$$Z_{0,\pm}^{(2),\mathrm{comp}} \sim \frac{2Z_{\mathrm{asym},\pm}^{\mathrm{kin}}}{|1 + R_\pm^{(0)} C_\pm \mathrm{i}\omega|^2} + 2\,\mathrm{Re}\,[Z_{\mathrm{CD},\pm}^{\mathrm{kin}} + Z_{0,\pm}^{\mathrm{OCP}} + Z_{0,\pm}^{\mathrm{W}}]. \tag{75}$$

Notice that these are close in form to the expressions 43, 49 and 56, but with capacitance modifying only the first term. Looking at the linear impedance 73, it now appears that the Warburg term is no longer in *parallel* with the capacitance (as in Fig. 4a) but in *series* (as in Fig. 4b). Since they each dominate at different frequency scales, the diffusion process interacts minimally with the kinetics. The same is true for the nonlinear impedances 74–75, where the terms that depend on the diffusion process separate out, leaving only the constant kinetic term $Z_{\mathrm{asym},\pm}^{\mathrm{kin}}$ (due to reaction asymmetry) in "parallel" with the capacitance. This simplifies the structure and interpretation of impedances, since the contribution of each nonlinearity can be more easily assessed.

Methods

Having introduced the model and analysed it in the frequency domain, we now detail the numerical, experimental and parameterization methods employed in the remainder of the paper to produce the results given in the Results section.

Numerical solution in the time domain for generation of synthetic data.—Here we describe the numerical methods for solving the SPM in the time domain and the procedure for generating synthetic impedance data from a known set of parameter values—this is useful for parameter identifiability and error sensitivity analysis (the Results section) because "ground truth" parameters are known exactly. Synthetic data was generated by solving the full nonlinear model Eqs. 15–24 in the time domain numerically given a sinusoidal input current of dimensional frequency ω^* and amplitude $2\hat{I}^*$ (or peak-to-peak amplitude $4\hat{I}^*$). This was then converted to the frequency domain with a Fourier transform. The radial dimension within the electrode particles was discretized using a finite volume scheme, and the time integration was performed using the adaptive explicit stiff ODE solver `ode15s` in MATLAB. To ensure sufficient relaxation of initial transients and convergence of the output voltage to a periodic profile, 20 periods were simulated and only the final 2 were selected to be fast Fourier transformed (FFT) with 20 equispaced samples per period. This procedure was performed for 30 frequencies logarithmically spaced from $\omega^* = 0.1$ mHz to 100 Hz, i.e. 5 frequencies per decade. The parameter set used corresponds to a LCO/LiC_6 cell, with values modified from Refs. 15, 29, summarized in Tables SI, SII of the supplementary material. Simulations were performed at three DoDs (30%, 50% and 70%) with a fixed current amplitude of 50 mA.

Zero-mean Gaussian noise was added to the simulated voltages in the frequency domain ($n = 1, 2$)

$$\widehat{V}_n^{*,\text{data}} = \widehat{V}_n^* + \varepsilon_n^*, \quad \varepsilon_n^* = \varepsilon_{n,r}^* + \mathrm{i}\varepsilon_{n,i}^*, \quad \text{where } \varepsilon_{n,r}^*, \varepsilon_{n,i}^* \sim N(0, \sigma_n^{*2}), \tag{76}$$

and the standard deviations were chosen to give similar signal-to-noise ratios to those seen in our experiments, i.e. $\sigma_1^* = \sigma_2^* = 10^{-7}$ V. The synthetic impedances were calculated from

$$Z_n^{*,\text{data}} = \frac{\widehat{V}_n^{*,\text{data}}}{(\hat{I}^*)^n}, \qquad n = 1, 2. \tag{77}$$

Experimental measurements.—Experiments were undertaken using a bespoke test rig to create an NLEIS dataset to parameterize the model. All measurements were collected in the time domain, then post-processed in MATLAB. A bipolar power source/sink (Kikusui PBZ60-6.7) was connected in series with an NMC/graphite pouch cell (Kokam SLPB533459H4, 740 mAh[30]) and a 0.1 Ω precision shunt resistor as shown in Fig. S1 in the supplementary material. Voltage measurements were made across the test battery and the shunt respectively using a 24-bit analog-to-digital converter (National Instruments 9239). Two cells were tested.

Prior to NLEIS experiments, the discharge capacity of each cell was measured at 19 °C and found to be 720 mAh and 729 mAh respectively. For capacity measurements, first a constant-current charge of 500 mA to 4.2 V was applied followed by a constant-voltage charge until the current dropped below 50 mA. Then, after a 30 min rest period, a constant-current discharge at 500 mA to a voltage of 2.7 V was conducted followed by a constant-voltage discharge to a current below 50 mA.

Nonlinear EIS measurements were collected at 10% DoD to 90% DoD (equivalently 90% SOC to 10% SOC), in steps of 10%. At each DoD, zero-mean sinusoidal currents of 1 A peak-to-peak were applied and voltage measurements taken at frequencies from 0.1 Hz to 10 kHz, with 10 measurements per decade. The length of the measurement was taken as the larger of 2 s or 20 cycles at each frequency. For more details on the procedures, including thermal limits, data acquisition and processing, see Section S4 of the supplementary material.

The measured voltage and current signals were each multiplied by a Hann window function, and then fast-Fourier transformed using MATLAB's built-in FFT function, giving the components $\widehat{V}_n(\omega, \hat{I})$ of the voltage as per 35.

OCP functions and electrode balancing.—Individual electrode OCPs $U_\pm^*$ for the Kokam SLPB533459H4 cells were determined from 3-electrode measurements by McTurk et al.,[28] who inserted a minimally invasive lithium reference electrode into cells of the same model. This data for $U_\pm^*$ is given in terms of normalised discharge capacity $Q = \text{DoD}/100$ with $Q \in [0, 1]$. For use with our model, analytical expressions (S4.6 of supplementary material) were fitted to the data, shown in Figs. 5a–5b. Figure 5c demonstrates that the resulting full-cell OCV agrees with the measured OCV of the cells used in this paper.

To balance the electrodes, the stoichiometry limits $c_\pm^{0\%}$ and $c_\pm^{100\%}$ corresponding to 0% and 100% DoD ($Q = 0$ and 1) were chosen using knowledge of the electrode chemistries. The resulting stoichiometry limits (and values of $\xi_\pm$ that follow from 33) are given later in Table I. Then $U_\pm^*$ is expressed in terms of $c_\pm$ using 32. When it is required, the first derivative of $U_\pm^*$ is calculated from the analytical fits, but the second derivative is calculated numerically from the OCP data. The OCP expressions and further details of the fitting procedures and electrode balancing are given in Section S4.6 of the supplementary material.

Parameter estimation.—To identify parameters and analyze their uniqueness, we consider fitting the (dimensional) model impedances $Z_n^{*,(n)} = \Phi^* Z_n^{(n)}/(J^*)^n$ to measured or simulated data $Z_n^{*,\text{data}}$ across a range of frequencies at a given DoD. The parameter estimation problem takes the form

$$\hat{\boldsymbol{\theta}} = \underset{\boldsymbol{\theta}}{\text{argmin}}\, l(\boldsymbol{\theta}), \tag{78}$$

where $\boldsymbol{\theta}$ is the vector of parameters to fit, and l is a loss function describing the goodness of fit. It is not obvious what loss function to use for NLEIS data since more than one impedance (i.e. Z_1^* and Z_2^*) is fitted simultaneously, and higher harmonics are typically smaller in magnitude but also more sensitive to some parameters. A straightforward choice of the total squared error across both harmonics would not account for this difference in scale or magnitude. Therefore, the relative weighting of the error across each harmonic merits consideration.

We take the approach of maximum likelihood estimation (MLE), assuming zero-mean Gaussian measurement noise added to the voltage harmonics, as in 76. Notably, we assume in general that the noise variances of the first and second harmonics are not the same. The details can be found in Section S5 of the supplementary material, and the resulting MLE for $\boldsymbol{\theta}$ given NLEIS data $Z_{1,j}^{*,\text{data}}$, $Z_{2,j}^{*,\text{data}}$ at frequencies ω_j, $j = 1, 2, \ldots, N_\omega$, is reduced to

$$\hat{\boldsymbol{\theta}}_{\text{NLEIS}} = \underset{\boldsymbol{\theta}}{\text{argmin}}(l_1(\boldsymbol{\theta}) + l_2(\boldsymbol{\theta})), \tag{79}$$

where

$$l_1(\boldsymbol{\theta}) = \log\left(\sum_{j=1}^{N_\omega} |Z_1^{*(1)}(\omega_j; \boldsymbol{\theta}) - Z_{1,j}^{*,\text{data}}|^2\right), \tag{80}$$

$$l_2(\boldsymbol{\theta}) = \log\left(\sum_{j=1}^{N_\omega} |Z_2^{*(2)}(\omega_j; \boldsymbol{\theta}) - Z_{2,j}^{*,\text{data}}|^2\right), \tag{81}$$

are the (negative) log-likelihoods, up to a scaling factor, from each harmonic. We will refer to their sum as the total loglikelihood $l_{12}(\boldsymbol{\theta}) = l_1 + l_2$. The form of l_{12}, which is the sum of the logarithm of the squared error of each harmonic, originates from the MLE process and has the advantage of being independent of the scale of each harmonic, as desired. That is, rescaling $(Z_n^{*n}, Z_n^{*,\text{data}}) \mapsto (aZ_n^{*n}, aZ_n^{*,\text{data}})$ for any a only changes l_{12} by an additive constant, leaving $\text{argmin}_{\boldsymbol{\theta}}\, l_{12}$ unchanged. Given only linear EIS data, consisting of $Z_{1,j}^{*,\text{data}}$, the corresponding MLE is

$$\hat{\boldsymbol{\theta}}_{\text{EIS}} = \underset{\boldsymbol{\theta}}{\text{argmin}}\, l_1(\boldsymbol{\theta}), \tag{82}$$

where the loss function is simply l_1.

The minimization problem 78 was solved using nonlinear optimization routines (local and global) in MATLAB employing bound constraints as described in Section S5 of the supplementary material.

Results

Analysis of model impedances.—We begin with an illustration of the form of the exact model impedances, up to second order, given by the formulae 61, 62 and 63. The dependence of $Z_{2,\pm}^{(2)}$ in particular on the various model parameters will be demonstrated. Then, the simplified (composite) formulae 73, 74 and 75 will be compared to the aforementioned exact results.

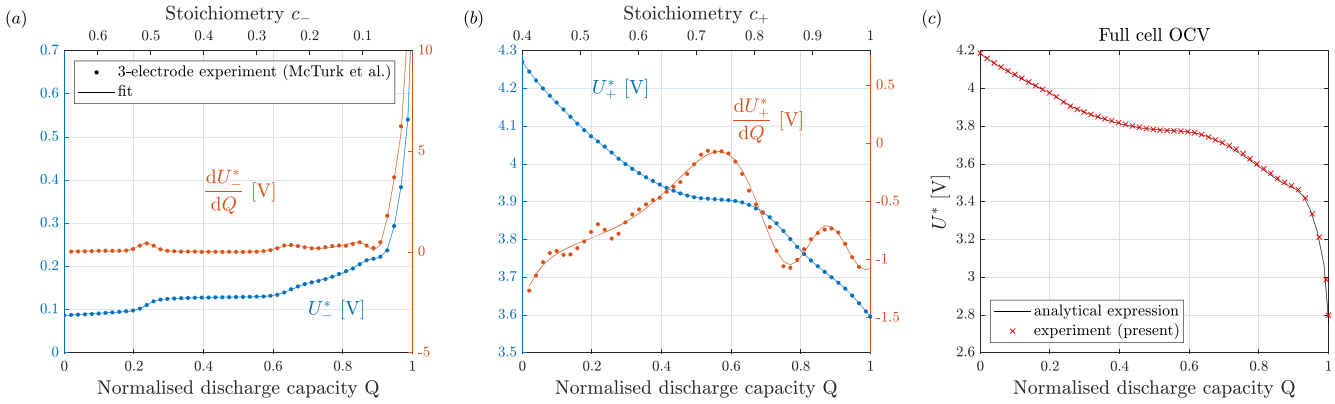

Figure 5. (a) Negative electrode OCP, (b) positive electrode OCP, and (c) full-cell OCV for a Kokam SLPB533459H4 740 mAh pouch cell. Dot markers are 3-electrode data from Ref. 28, solid lines are analytical expressions (Eqs. (S4.1), (S4.2) in supplementary material) that were fitted to individual electrode OCP data. Panel (*c*) compares these fits to the measured full-cell OCV for the present cells from which NLEIS data was collected.

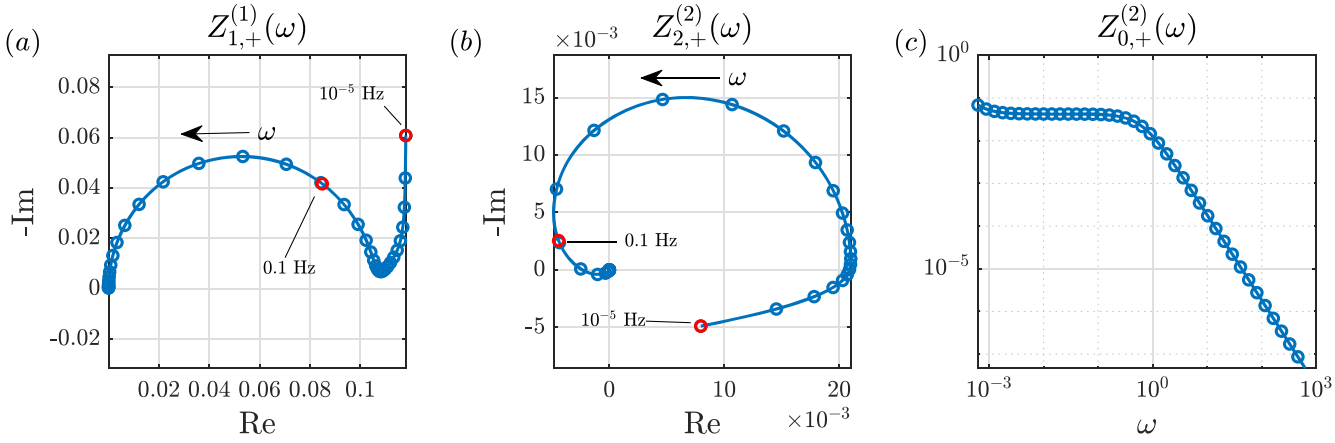

Figure 6. Nyquist plot of the fundamental (linear) impedance $Z_{1,+}^{(1)}$, and the second-order nonlinear impedances $Z_{2,+}^{(2)}$ (second harmonic) and $Z_{0,+}^{(2)}$ (zero frequency mode), as calculated from formulae 61, 62 and 63. Parameters in Table SII at DoD = 30% (i.e. $c_+ = 0.80$). Frequency range is $10^{-4} \leqslant \omega/2\pi \leqslant 10^{2}$ [Hz], with 5 values (marked) per decade. Only the impedances for positive electrode shown.

Table I. Parameter group values estimated from EIS and NLEIS data, which are used for model validation in Fig. 17. The $\chi_\pm$ parameters are interpolated on the values in Figs. 15a, 15b for different DoDs (NLEIS estimates used are the red markers). From our impedance measurements the series resistance is $R_s^* = 9.2$ mV ($R_s = 0.358$), but for the model validation (Fig. 17) we use $R_s^* = 20$ mV and $R_s = 0.779$.

Parameter groups	Negative (−)		Positive (+)	
	EIS estimate	NLEIS estimate	EIS estimate	NLEIS estimate
$\chi_\pm$	Fig. 15a	Fig. 15a	Fig. 15b	Fig. 15b
$\beta_\pm$	0.5	0.496	0.5	0.482
$C_\pm$	1.528×10^{-3}	2.589×10^{-3}	1.747×10^{-2}	2.645×10^{-2}
$\tau_{d,\pm}$	1.571×10^{4}	1.570×10^{3}	1.227×10^{5}	1.185×10^{5}
$\xi_\pm$	8.126×10^{-5}		7.414×10^{-5}	
$c_\pm^{0\%}$	0.664		0.40	

Typical Nyquist plots of the impedances $Z_{1,+}^{(1)}$, $Z_{2,+}^{(2)}$ and $Z_{0,+}^{(2)}$ are shown in Fig. 6, using the parameter values in Tables SI, SII in the supplementary material. (Only the positive electrode impedances are shown—negative electrode ones have a similar structure.) In Fig. 6a, $Z_{1,+}^{(1)}$ consists of a high frequency semi-circular kinetic arc, and a low frequency diffusive tail with a capacitive effect ($Z_{1,+}^{(1)} = O(1/\omega)$) as $\omega \to 0$. That is, the same as the well-understood Randles circuit with finite-space diffusion. In Fig. 6b, we see the second harmonic impedance $Z_{2,+}^{(2)}$ also consists of a high frequency kinetic arc and diffusive tail, but this arc appears "spiral" in nature rather than circular. Equation 70 (region II) describes this and, excluding the factor of $(1 + 2R_\pm^{(0)} C_\pm \mathrm{i}\omega)$ (which affects mainly the shape close to the origin), shows that $Z_{2,+}^{(2)}$ is proportional to the square of the semi-circular kinetics in $Z_{1,\pm}^{(1)}$, resulting in a *cardioid*-like shape. Lastly, the second-order correction at the zeroth harmonic, $Z_{0,+}^{(2)}$, contains similar model information as $Z_{2,+}^{(2)}$ but with no imaginary component. In Fig. 6c, we see $Z_{0,+}^{(2)} = O(\omega^{-2})$ at high frequencies (square of

double-layer capacitive effects) but also begin to see this behavior at low frequencies (square of electrode "differential capacitive" effects). However, in intermediate regions $Z^{(2)}_{0,+}$ appears relatively flat and the various effects are difficult to delineate.

Next, we demonstrate in Fig. 7 how the various features of $Z^{(2)}_{2,+}$ (and therefore $Z^{(2)}_{2,-}$) depend on quantities in the model. Starting from the values in Tables SI, SII and at 30% DoD, we varied $R^{(0)}_{+}$, C_{+}, $R^{(0)\prime}_{+}$, β_{+}, $\tau_{\mathrm{d},+}$, and $U^{(0)\prime\prime}_{+}$ across a representative range (considering both positive and negative values for the derivatives $R^{(0)\prime}_{+}$, $U^{(0)\prime\prime}_{+}$). From Fig. 7 we observe that:

(a) $R^{(0)}_{+}$ affects the size of the kinetic arc (its "width" on the real axis is $Z^{\mathrm{kin}}_{\mathrm{asym},+} = (\beta_{+} - 1/2)(R^{(0)}_{+})^2$);
(b) C_{+} affects the frequency dependence of the kinetic arc, but not its shape (just as for $Z^{(1)}_{1,+}$);
(c) $R^{(0)\prime}_{+}$ affects the initial direction and magnitude of the diffusion tail (due to $Z^{\mathrm{kin}}_{\mathrm{CD},+}$) emanating from the kinetic arc;
(d) β_{+} affects the size (via the magnitude $|\beta_{+} - 1/2|$) and orientation (via $\mathrm{sgn}(\beta_{+} - 1/2)$) of the kinetic arc (see point (*a*) above). Important to note that as $\beta_{+} \to 1/2$ the totality of the arc shrinks to the origin. Thus $\beta_{+} \neq 1/2$ is *necessary* to observe an arc at all (this was first pointed out by Murbach et al.[5]);
(e) $\tau_{\mathrm{d},+}$ affects the length and shape of the diffusion tail (via the terms $Z^{\mathrm{kin}}_{\mathrm{CD},+}$ and Z^{OCP}_{+});
(f) $U^{(0)\prime\prime}_{+}$ affects whether the diffusion tail ultimately diverges to $\mathrm{Re} = -\infty$ (when $U^{(0)\prime\prime}_{+} > 0$) or $\mathrm{Re} = +\infty$ (when $U^{(0)\prime\prime}_{+} < 0$) as $\omega \to 0$.

It is clear that the possible behavior of $Z^{(2)}_{2,+}$ is much more varied than $Z^{(1)}_{1,+}$, with visible signatures of many quantities in the model that are not visible with EIS, e.g. β_{+}, $R^{(0)\prime}_{+}$, and $U^{(0)\prime\prime}_{+}$. In addition, dependence of $Z^{(2)}_{2,+}$ on $R^{(0)}_{+}$, C_{+} and $\tau_{\mathrm{d},+}$ gives further information that may be used to improve their identifiability over traditional linear EIS.

Finally, we remark on the accuracy of the simplified (composite) expressions 73, 74 and 75, which assume that the capacitive timescale $R^{(0)}_{\pm}C_{\pm}$ is much shorter than the diffusive one, $\tau_{\mathrm{d},\pm} = 1/D^{(0)}_{\pm}$. Comparing these to the exact impedances for a full-cell, we find them practically indistinguishable—across all frequencies and each harmonic—with mean relative errors less than 0.03% for the fundamental and 0.64% for the second harmonic. Details are given in Section S6 of the supplementary material. Consequently, these composite expressions are a useful and simple substitute for the full expressions in practice.

Structural parameter identifiability.—Nine dynamical parameter groups 34 are sufficient to fully parameterize the nonlinear SPM 15–24. However, these parameters are not necessarily able to be determined uniquely (or at all) from the model structure. This problem is referred to as structural parameter identifiability,[31] and we will consider the improvements that NLEIS provides relative to linear EIS.[24]

Structural identifiability is typically defined for linear systems, but here we will use a nonlinear extension. Consider a set of nonlinear impedances $\{Z^{(1)}_{1}(\omega, \boldsymbol{\theta}), Z^{(2)}_{2}(\omega, \boldsymbol{\theta}), \ldots\}$, characterising a nonlinear model in the frequency domain, for parameters $\boldsymbol{\theta} \in \Theta$. If the system of Eqs. with $\boldsymbol{\theta}, \tilde{\boldsymbol{\theta}} \in \Theta$

$$Z^{(1)}_{1}(\omega, \boldsymbol{\theta}) = Z^{(1)}_{1}(\omega, \tilde{\boldsymbol{\theta}}), \qquad [83]$$

$$Z^{(2)}_{2}(\omega, \boldsymbol{\theta}) = Z^{(2)}_{2}(\omega, \tilde{\boldsymbol{\theta}}),$$
$$\vdots \qquad [84]$$

for all $\omega \in \mathbb{R}$, has: (i) a unique solution for $\boldsymbol{\theta}$, then the model is globally identifiable; (ii) a finite number of solutions for $\boldsymbol{\theta}$, it is locally identifiable; (iii) an infinite number of solutions for $\boldsymbol{\theta}$, it is unidentifiable.

Single electrode.—First, we will consider the parameter identifiability of a single electrode (positive or negative) and restrict ourselves to the accurate simplified formulae 73–74. For a single ($\pm$) electrode, the relevant unknown parameters are $\chi_{\pm}$, $C_{\pm}$, $\beta_{\pm}$, $\tau_{\mathrm{d},\pm}$, but for convenience we will consider

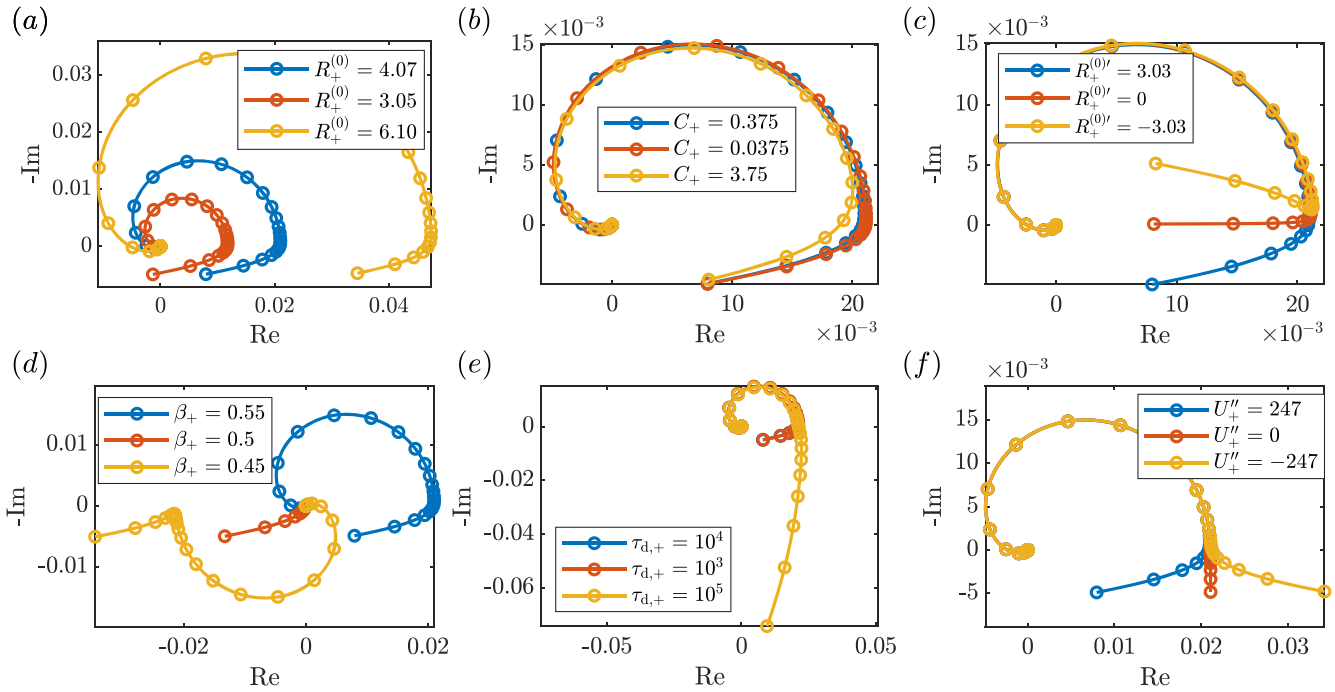

Figure 7. Dependence of the second harmonic impedance $Z^{(2)}_{2,+}$ on quantities (*a*) $R^{(0)}_{+}$, (*b*) C_{+}, (*c*) $R^{(0)\prime}_{+}$, (*d*) β_{+}, (*e*) $\tau_{\mathrm{d},+}$, (*f*) $U^{(0)\prime\prime}_{+}$. For each, we used the value in Table SII (at DoD = 30%), shown in blue, and 2 other representative values.

$$R_{\pm}^{(0)} = \frac{2\chi_{\pm}}{(c_{\pm}^{(0)})^{\beta_{\pm}}(1-c_{\pm}^{(0)})^{1-\beta_{\pm}}}, \qquad [85]$$

in place of $\chi_{\pm}$, and discuss identifiability of $\chi_{\pm}$ subsequently.

For a single electrode, if only $Z_{1,\pm}^{(1)}$ is given, 73 shows that $R_{\pm}^{(0)}$, $C_{\pm}$ have unique solutions (globally identifiable), and so does $\tau_{\mathrm{d},\pm}$ provided $U_{\pm}^{(0)'} \neq 0$. If $U_{\pm}^{(0)'} = 0$, i.e. if the OCP slope is exactly zero, the diffusive contribution to the impedance vanishes and $\tau_{\mathrm{d},\pm}$ is unidentifiable—as per Bizeray et al.[24] for Fickian diffusion. However, the charge transfer coefficient $\beta_{\pm}$ does not appear in $Z_{1,\pm}^{(1)}$ and is therefore always unidentifiable. In this case $\chi_{\pm}$ cannot be identified from 85, leaving only $R_{\pm}^{(0)}$ identified.

However, if the second harmonic is also considered, i.e., $\{Z_{1,\pm}^{(1)}, Z_{2,\pm}^{(2)}\}$ is given, then more information on each parameter is provided. In particular, $\beta_{\pm}$ (and hence $\chi_{\pm}$) becomes globally identifiable since it appears explicitly in $Z_{2,\pm}^{(2)}$. Regarding the diffusion timescale $\tau_{\mathrm{d},\pm}$: if $U_{\pm}^{(0)'} = 0$ (hence $\tau_{\mathrm{d},\pm}$ unidentifiable from $Z_{1,\pm}^{(1)}$ alone) but $U_{\pm}^{(0)''} \neq 0$, then the terms $Z_{\pm}^{\mathrm{OCP}}$ and $Z_{\pm,2}^{\mathrm{W}}$ in $Z_{2,\pm}^{(2)}$ do not vanish and in fact make $\tau_{\mathrm{d},\pm}$ identifiable. However, if $U_{\pm}^{(0)''} = 0$ also, then $\tau_{\mathrm{d},\pm}$ remains unidentifiable.

Full two-electrode cell.—Given the impedances $\{Z_{1,\pm}^{(1)}, Z_{2,\pm}^{(2)}\}$ for a single electrode, the full cell impedances are given by 64–65 and they inherit each electrode's structural identifiability since no parameters appear in impedances from *both* electrodes. However, they may have additional identifiability issues arising from cell symmetries, i.e., "electrode swapping", or inability to decide whether a parameter refers to the positive or negative electrode.

If the full-cell linear impedance $Z_1^{(1)} = Z_{1,+}^{(1)} - Z_{1,-}^{(1)} + R_s$ is given, the series resistance R_s is unique (globally identifiable) and can be extracted from the high frequency limit $\omega \to \infty$, where $Z_1^{(1)} \to R_s$. However, the identifiable kinetic parameters now have two solutions: if $(R_-^{(0)}, C_-, R_+^{(0)}, C_+)$ is a solution then so is $(R_+^{(0)}, C_+, R_-^{(0)}, C_-)$. Hence they are only *locally* identifiable. A similar symmetry exists for the diffusion timescales $\tau_{\mathrm{d},\pm}$ but only for special values of the OCP slopes. Substituting 73 into condition 83, and keeping only the Warburg terms, gives (recall $D_{\pm}^{(0)} = -U_{\pm}^{(0)'}c_{\pm}^{(0)}/\tau_{\mathrm{d},\pm}$):

$$\begin{aligned}&\frac{\xi_+ U_+^{(0)'}}{D_+^{(0)}} H_1\left(\frac{\omega}{D_+^{(0)}}\right) + \frac{\xi_- U_-^{(0)'}}{D_-^{(0)}} H_1\left(\frac{\omega}{D_-^{(0)}}\right)\\ &= \frac{\xi_+ U_+^{(0)'}}{\tilde{D}_+^{(0)}} H_1\left(\frac{\omega}{\tilde{D}_+^{(0)}}\right) + \frac{\xi_- U_-^{(0)'}}{\tilde{D}_-^{(0)}} H_1\left(\frac{\omega}{\tilde{D}_-^{(0)}}\right).\end{aligned} \qquad [86]$$

If the OCP slopes are nonzero and satisfy $\xi_+ U_+^{(0)'} = \xi_- U_-^{(0)'}$, this reduces to

$$\begin{aligned}&\frac{1}{D_+^{(0)}} H_1\left(\frac{\omega}{D_+^{(0)}}\right) + \frac{1}{D_-^{(0)}} H_1\left(\frac{\omega}{D_-^{(0)}}\right)\\ &= \frac{1}{\tilde{D}_+^{(0)}} H_1\left(\frac{\omega}{\tilde{D}_+^{(0)}}\right) + \frac{1}{\tilde{D}_-^{(0)}} H_1\left(\frac{\omega}{\tilde{D}_-^{(0)}}\right).\end{aligned} \qquad [87]$$

The left hand side has the symmetry $D_-^{(0)} \mapsto D_+^{(0)}$, $D_+^{(0)} \mapsto D_-^{(0)}$, meaning there are always two solutions for $(D_+^{(0)}, D_-^{(0)})$ and hence $(\tau_{\mathrm{d},+}, \tau_{\mathrm{d},-})$. This symmetry in terms of $\tau_{\mathrm{d},\pm}$ is

$$\tau_{\mathrm{d},+} \mapsto \frac{U_+^{(0)'}c_+^{(0)}}{U_-^{(0)'}c_-^{(0)}}\tau_{\mathrm{d},-}, \qquad \tau_{\mathrm{d},-} \mapsto \frac{U_-^{(0)'}c_-^{(0)}}{U_+^{(0)'}c_+^{(0)}}\tau_{\mathrm{d},+}. \qquad [88]$$

This electrode symmetry of diffusion timescales in $Z_1^{(1)}$ was pointed out by Bizeray et al.,[24] which we extend here to the case of nonlinear diffusion.

If the full-cell second harmonic is also considered, i.e., $\{Z_1^{(1)}, Z_2^{(2)}\}$ is given, the above symmetries are removed in most cases. Substituting 74 into condition 84, as H_1, H_1^2 and H_2 are distinct functions of ω, the diffusion symmetry $D_-^{(0)} \mapsto D_+^{(0)}$, $D_+^{(0)} \mapsto D_-^{(0)}$ only holds (using similar arguments to 86–87) if $\xi_+^2 U_+^{(0)''} = -\xi_-^2 U_-^{(0)''}$ and $\xi_+^2 U_+^{(0)'}/c_+^{(0)} = -\xi_-^2 U_-^{(0)'}/c_-^{(0)}$. But we already require $\xi_+ U_+^{(0)'} = \xi_- U_-^{(0)'}$ from $Z_1^{(1)}$ which, if $U_{\pm}^{(0)'} \neq 0$, reduces the latter to $\xi_+/c_+^{(0)} = -\xi_-/c_-^{(0)}$, and this is not possible since ξ_+ and ξ_- are both positive. If actually $U_{\pm}^{(0)'} = 0$, then the symmetry can persist so long as $\xi_+^2 U_+^{(0)''} = -\xi_-^2 U_-^{(0)''}$.

If the diffusion symmetry is removed, then the terms $Z_{\pm,\mathrm{CD}}^{\mathrm{kin}}$ (see 51) prevent the symmetry in $R_{\pm}^{(0)}$, $C_{\pm}$ too as they depend on both kinetic and diffusive parameters. However, in the special case of $R_-^{(0)'} = R_+^{(0)'} = 0$, i.e. both exchange current densities are independent of concentration (at this DoD), then $Z_{\pm,\mathrm{CD}}^{\mathrm{kin}}$ vanishes and a symmetry in the kinetic parameters does persist, given by $R_{\pm}^{(0)} \mapsto R_{\mp}^{(0)}$, $C_{\pm} \mapsto C_{\mp}$, $\beta_{\pm} \mapsto 1-\beta_{\mp}$.

In summary, including the second harmonic $Z_2^{(2)}$, makes $\beta_{\pm}$ (and hence $\chi_{\pm}$) globally identifiable, and improves the identifiability of the diffusion timescales $\tau_{\mathrm{d},\pm}$ when an OCP is flat ($U_{\pm}^{(0)'} = 0$) but has nonzero curvature ($U_{\pm}^{(0)''} \neq 0$). In addition, it removes the electrode swapping symmetries in general, except when both OCVs are flat ($U_+^{(0)'} = U_-^{(0)'} = 0$) or both exchange current densities are independent of concentration ($R_-^{(0)'} = R_+^{(0)'} = 0$).

Parameter estimation from synthetic data.—With the structural identifiability from the first two harmonics analysed, we move to analyze the practical identifiability, i.e. parameter estimation from data. In this section, we consider noisy synthetic data from a known parameter set—see the Methods Section for the generation method and parameter values. The parameter estimation algorithm from EIS data ($Z_1^{*,\mathrm{data}}$ only) and NLEIS data ($Z_1^{*,\mathrm{data}}$ and $Z_2^{*,\mathrm{data}}$) was given in the Methods Section and results in estimators $\hat{\boldsymbol{\theta}}_{\mathrm{EIS}}$, $\hat{\boldsymbol{\theta}}_{\mathrm{NLEIS}}$ for the parameter groups.

To test the consistency and noise sensitivity of our approach we repeatedly applied the estimation algorithm to synthetic data but each time with separate samples drawn from the noise distribution (given in 76). This resampling, known as "bootstrapping",[32] allows the construction of the distribution of the estimators $\hat{\boldsymbol{\theta}}_{\mathrm{EIS}}$, $\hat{\boldsymbol{\theta}}_{\mathrm{NLEIS}}$. The distributions (histograms) and their means for 200 resamples are shown and compared in Figs. 8 (with data at 50% DoD) and 9 (at 70% DoD). Note that the transfer coefficient $\beta_{\pm}$ is unidentifiable from EIS data and thus only estimates from NLEIS data are shown. Also, although NLEIS data can be used to estimate the typical non-dimensional charge transfer resistance $\chi_{\pm}$, EIS data cannot, so to compare methods we plot the charge transfer resistances $R_{\pm}^{(0)}$ instead.

Figures 8 and 9 show that the mean and variance of the kinetic parameter estimators $R_{\pm}^{(0)}$, $C_{\pm}$ are similar in all cases. The NLEIS-based estimator of β_+ has low variance, but that for β_- has high variance. This is due to the resistance of the negative electrode ($R_-^{(0)}$)

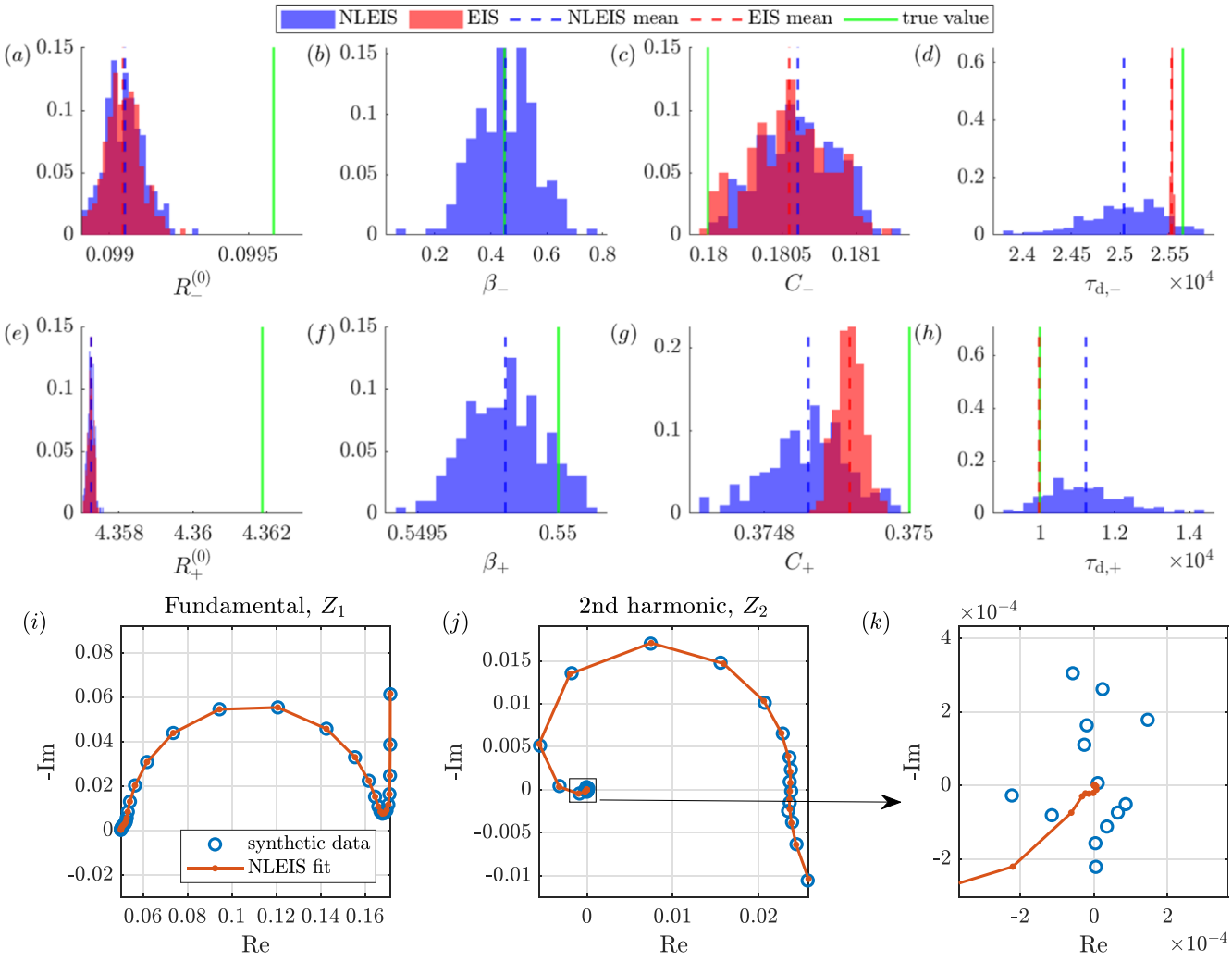

Figure 8. (50% DoD) Parameter distributions (histograms) for $\hat{\boldsymbol{\theta}}_{\text{NLEIS}}$ from repeated fitting to synthetic NLEIS data, showing sensitivity to error (a)–(h). Distributions for fitting $\hat{\boldsymbol{\theta}}_{\text{EIS}}$ to just EIS data (fundamental only) also shown. Dashed lines are mean values, with true ones shown in green. Estimates for $\beta_\pm$ not shown for EIS as they are not identifiable. Example impedance fit shown in (i)–(k), including blown-up plot (k) of Z_2 near the origin.

being much lower than that of the positive, hence its kinetic cardioid spiral in Z_2^* is much smaller in magnitude, and affected more by noise—see Figs. 8j–8k. The discrepancy between the means and the true values (i.e. estimator bias) is due to the small-current-amplitude approximation we used to derive the model impedances. We determined this by fitting to synthetic data generated using smaller current amplitudes and found that the bias reduced. This bias thus represents model error rather than noise, as the data generation used a finite amplitude.

The diffusion timescales $\tau_{d,\pm}$ are more influenced by noise, with the NLEIS estimates showing larger variance than the EIS ones. However, this variance is comparable to the model error—the EIS estimates of $\tau_{d,\pm}$ can be overly confident (low variance), despite having a similar model error to NLEIS (Fig. 9 for 70% DoD).

Log-likelihood analysis of diffusion timescales.—A clearer understanding of the practical identifiability of diffusion time $\tau_{d,\pm}$ can be reached by looking at the log-likelihoods (i.e. the cost functions associated with the parameter estimation problem) for each harmonic directly, $l_1(\boldsymbol{\theta})$, $l_2(\boldsymbol{\theta})$ in the $(\tau_{d,+}, \tau_{d,-})$ plane. Figure 10 shows these (and the full log-likelihood $l_{12} = l_1 + l_2$) at 3 DoDs, with kinetic parameters fixed at their true values.

The shape of the l_1 landscape (Figs. 10a, 10d, 10g) depends on OCP slopes $U_\pm^{(0)'}$, as discussed in detail by Bizeray et al.[24] (for Fickian diffusion, but the structure is qualitatively the same). When one of the OCP slopes $U_\pm^{(0)'}$ is small, a valley in l_1 appears through the minimum, showing poor identifiability of the corresponding $\tau_{d,\pm}$. Of the results shown, the negative electrode OCP slope $|U_-^{(0)'}|$ is largest (≈17.9) at 50% DoD, where $\tau_{d,-}$ identifiability is best, and smallest (≈0.36) at 30% DoD, where it is worst. But the positive electrode OCP slope $|U_+^{(0)'}|$ is largest (≈18.0) at 30% DoD and decreases at 50% DoD (≈6.5) and 70% DoD (≈2.2), decreasing $\tau_{d,+}$ identifiability. At 70% DoD, $|U_-^{(0)'}| \approx |U_+^{(0)'}|$, giving electrode symmetry (see the Structural Parameter Identifiability section), and 2 local minima in l_1. The red line on the l_1 plots is the relationship between $\tau_{d,-}$ and $\tau_{d,+}$ if both slopes $U_-^{(0)'}$, $U_+^{(0)'} \to 0$, in which case 86 reduces to, at leading order,

$$A_+\sqrt{\tau_{d,+}} + A_-\sqrt{\tau_{d,-}} = \text{const.}$$
$$\text{where } A_\pm = \xi_\pm\sqrt{\frac{|U_\pm^{(0)'}|}{c_\pm^{(0)}}}. \qquad [89]$$

This gives a visual guide to the predominant structure of the l_1 landscape.

For the log-likelihood $l_2(\boldsymbol{\theta})$ of the second harmonic (Fig. 10b, 10e, 10h), its landscape depends on $U_\pm^{(0)'}$, $U_\pm^{(0)''}$ and $R_\pm^{(0)'}$ and so is more difficult to predict from the formulae, but crucially it is distinct

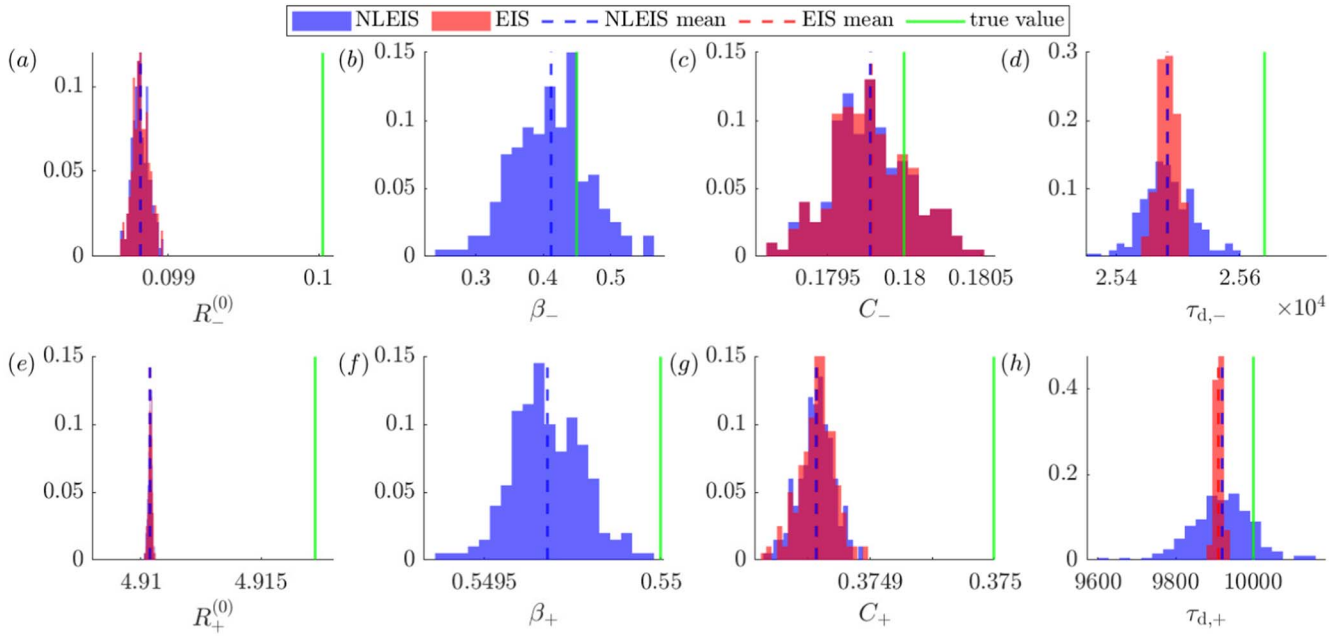

Figure 9. (70% DoD) Parameter distributions (histograms) for $\hat{\boldsymbol{\theta}}_{\text{NLEIS}}$ from repeated fitting to synthetic NLEIS data, showing sensitivity to error. See caption for Fig. 8.

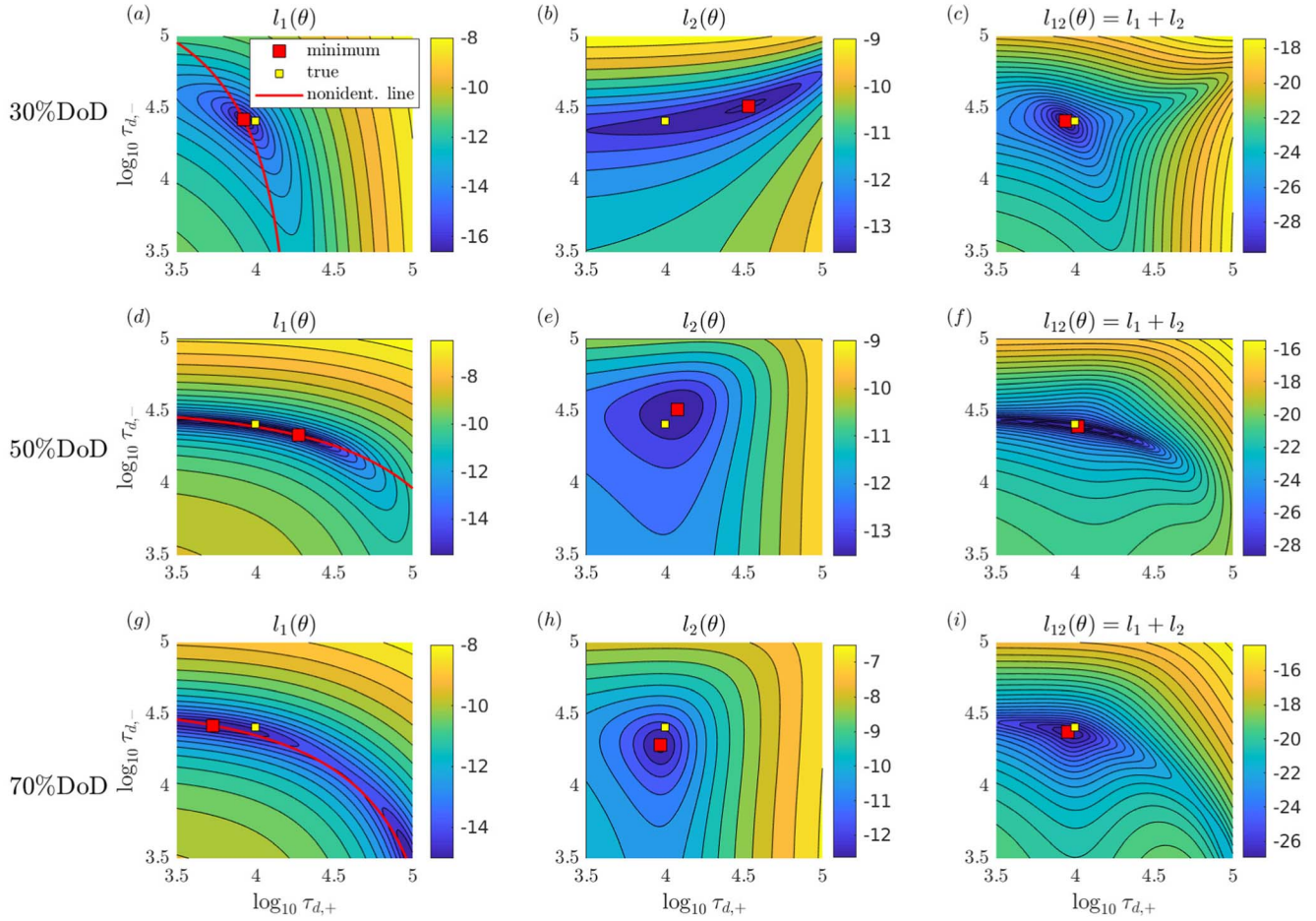

Figure 10. Synthetic data: Log-likelihood plotted in the $\tau_{d,+}$ and $\tau_{d,-}$ plane (other parameters fixed at true values). DoD (indicated) increases from top row to bottom row. Left column is log-likelihood l_1 for $Z_1^{(1)}$ only; middle column is log-likelihood l_2 for $Z_2^{(2)}$ only; right column is the total log-likelihood $l_{12} = l_1 + l_2$. For 30%, 50%, 70% DoD we have $-U_-^{(0)'} \approx 0.4$, 17.9, 1.6, and $-U_+^{(0)'} \approx 18.0$, 6.5, 2.2. Red line is 89.

from the landscape of l_1. Thus, when it is combined with l_1 to produce the total log-likehood l_{12}, the identifiability of the pair ($\tau_{\mathrm{d},+}$, $\tau_{\mathrm{d},-}$) is improved. For example, at 50% and 70% DoD, identifiability of $\tau_{\mathrm{d},+}$ is improved, and the second minimum (at 70%) eliminated. In each case, including l_2 moves the global minimum closer to the true value. We make an additional remark that the minima of l_1 in Fig. 10 are further from the true value than the estimates in Fig. 8. This is because, in the latter, the kinetic parameters were fitted simultaneously which allowed a better estimate of the diffusion times (i.e. reduced the bias due to the small current amplitude expansion). As kinetic parameters were fixed at their true values in Fig. 10, this bias is increased for the diffusion times. Using fitted kinetic parameters in Fig. 10 instead, the minima move closer to the true values. However, this highlights the high sensitivity of linear EIS estimates to errors in the kinetic parameters.

Lastly, relevant for fitting to experimental data in the next section, we consider the case where OCP curvature $U_{\pm}^{(0)''}$ is not known, due to measurement error and difficulties associated with approximating second derivatives numerically from noisy data. In this case, Fig. 11 shows l_1, l_2, l_{12} where, for each pair of values ($\tau_{\mathrm{d},+}$, $\tau_{\mathrm{d},-}$), we have minimised over $U_{-}^{(0)''}$ and $U_{+}^{(0)''}$—this corresponds to constructing "profile likelihoods" where $U_{-}^{(0)''}$, $U_{+}^{(0)''}$ are nuisance parameters that are not of interest.[33,34] Note that l_1 is unchanged from Fig. 10 as it does not depend on $U_{\pm}^{(0)''}$. Even here, with no knowledge of $U_{\pm}^{(0)''}$, the second harmonic provides enough information to improve identifiability over the fundamental alone.

In Fig. 11, the dashed overlaid line corresponds to $\tau_{\mathrm{d},-} = (c_{+}^{(0)}U_{+}^{(0)'})\tau_{\mathrm{d},+}/(c_{-}^{(0)}U_{-}^{(0)'})$ (or $D_{-}^{(0)} = D_{+}^{(0)}$) along which the pair $U_{-}^{(0)''}$, $U_{+}^{(0)''}$ are unidentifiable. This was verified by investigating the $(U_{-}^{(0)''}, U_{+}^{(0)''})$ plane when $(\tau_{\mathrm{d},+}, \tau_{\mathrm{d},-})$ are on this dashed line. However, this only introduces small numerical irregularities which are irrelevant if far from the global minimum.

Parameter estimation from experimental data.—We have explored the parameter estimation approach and advantages of NLEIS using synthetic data, and now turn to experimental data collected from an NMC cathode/graphite anode cell—see the Experimental Methods Section for details. We consider data collected at 10%, 20%, ..., 90% DoD, at each of which we consider EIS (Z_1^* only) and NLEIS (Z_1^* and Z_2^*) model fits.

The fits to EIS data are shown first, in Fig. 12, with the associated parameter estimates in Fig. 15. The model is able to fit the semi-circular reaction kinetics well, although we do not expect to capture the very high frequency behavior as our model does not include phenomena such as transport through SEI layers, relevant for $\omega^* \gtrsim 1$ kHz. We can extract the series resistance as the high frequency intercept with the real axis, giving $R_s^* = 9.2\,\mathrm{m}\Omega$ (and dimensionless $R_s = 0.358$). As discussed in the Structural Parameter Identifiability section, estimating kinetics from EIS data suffers from an inability to determine which electrode the parameters correspond to. Hence, we made the assumption that the larger charge transfer resistance (radius of semi-circle) was due to the positive electrode, but this was arbitrary and did not affect the goodness of fit. Note also that β_- and β_+ cannot be determined at all, so we set them equal to 1/2, as is typically done implicitly in other studies.

The diffusion tails are fitted reasonably well. However the corresponding timescales show extreme variation with DoD, up to

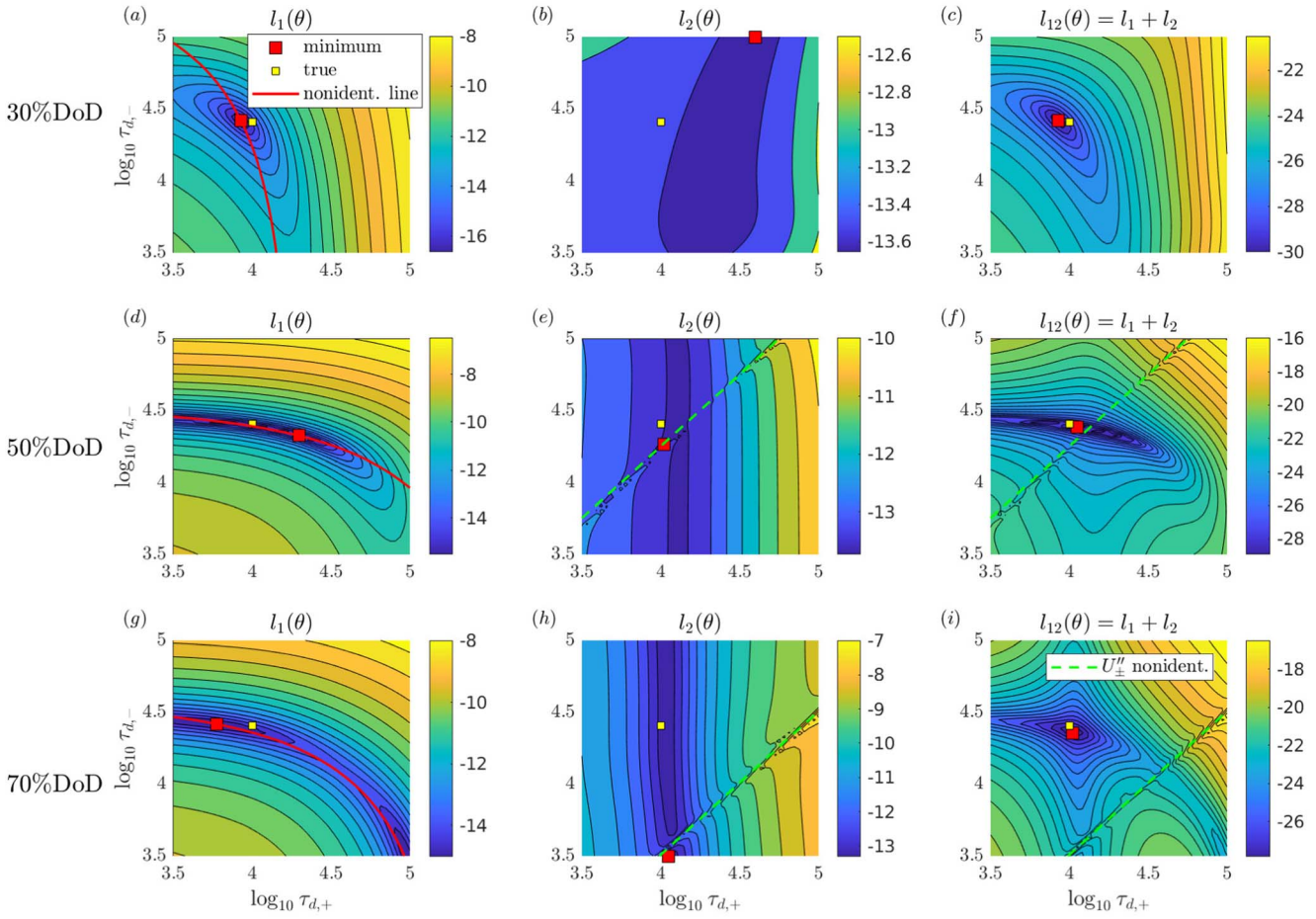

Figure 11. Synthetic data: Log-likelihood plotted in the $\tau_{d,+}$ and $\tau_{d,-}$ plane. Same as Fig. 10, but at each ($\tau_{d,+}$, $\tau_{d,-}$) pair, we minimize l_2 over $U_{+}^{(0)''}$ and $U_{-}^{(0)''}$. Dashed line is $\tau_{\mathrm{d},-} = (c_{+}^{(0)}U_{+}^{(0)'})\tau_{\mathrm{d},+}/(c_{-}^{(0)}U_{-}^{(0)'})$ (or $D_- = D_+$) where $U_{\pm}^{(0)''}$ are unidentifiable.

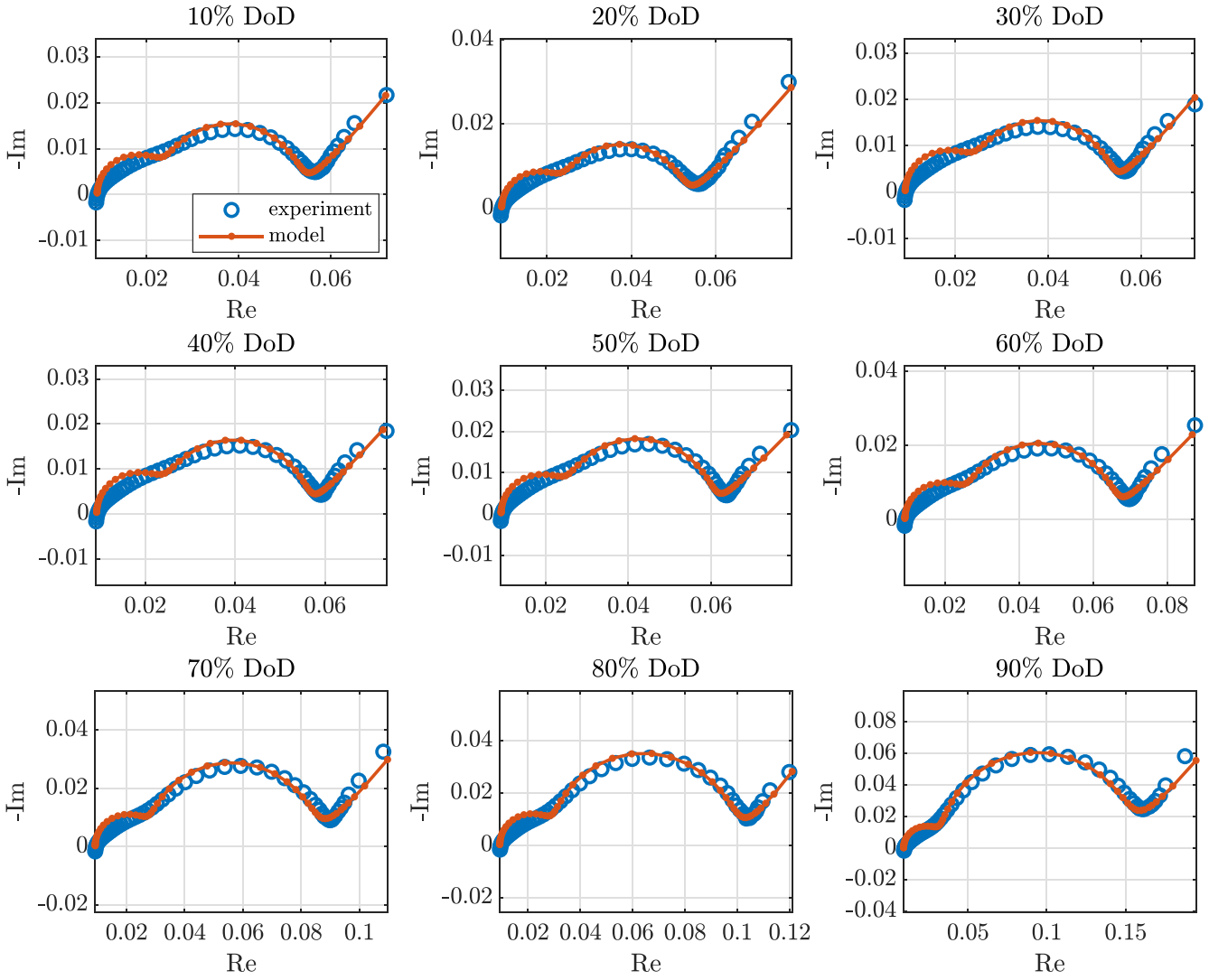

Figure 12. Fits of the model fundamental impedance $Z_1^{(1)*}$ to corresponding experimental fundamental impedance data. Units are in Ohms (VA^{-1}). Fits performed at each DoD in the range 10%, 20%,… 90% are shown, for the frequency range $f^* = 0.01 - 500$ Hz. Parameter estimates are given in Fig. 15.

4 orders of magnitude—as is usually seen when estimating diffusion parameters from EIS or GITT data.[35–37] As we will see, NLEIS can be a more sensitive tool for probing the validity of the underlying diffusion model.

Next, fits to NLEIS data (Z_1^* and Z_2^* simultaneously) are shown in Fig. 13 (with parameters in Fig. 15). We consider two cases: (i) using values of $U_\pm^{(0)''}$ calculated from Fig. 5, and; (ii) fitting $U_\pm^{(0)''}$, assuming they are not known a priori, or are inaccurate. In both cases, the reaction kinetics in each harmonic are captured very well for each DoD, as shown by the semi-circles in Z_1^* and cardioid spirals in Z_2^*. The resulting values for $\beta_\pm$, $C_\pm$, $\chi_\pm$ also do not vary appreciably across DoD except χ_+, suggesting the functional form of the exchange current density 6 is less appropriate for that electrode. The charge transfer coefficients $\beta_\pm$ both only slightly deviate from the symmetric value of 1/2 for these cells. Here β_+ deviates most from 1/2 and is responsible for the predominant cardioid in Z_2^*. The cardioid from the negative electrode is small and only visible by zooming in closer to the origin—see Fig. 14. The effect of noise in the second harmonic becomes significant (signal-to-noise ratio is low) above approximately 1 Hz, which is visible in Fig. 14. Noise was negligible in the first harmonic measurements.

Regarding the low frequency diffusion tails, the model fits are less convincing. When $U_\pm^{(0)''}$ is assumed known, the tail in Z_2^* may point in the opposite direction (10%, 20%, 50% DoD) or have the wrong length (30%, 40%). Also, the tail in Z_1^* is now too short in some cases (40%, 50%, 60%). However, if OCP curvatures $U_\pm^{(0)''}$ are allowed to be fitted instead, the fit to the tail in Z_2^* is significantly improved. Also, the tail in Z_1^* and the fit to the kinetic portions are improved; see the zoom-ins of Fig. 14. This suggests, even if only the *kinetic* parameters are of interest, fitting $U_\pm^{(0)''}$ may be better than prescribing inaccurate values. The resulting diffusion timescales (Figs. 15c, 15d) also show the least variation with DoD for NLEIS data fits when $U_\pm^{(0)''}$ is fitted (red), an improvement over the EIS data fits (blue), and hence closer to the model assumption that it is does not vary with DoD.

Supporting the conclusions presented above, the relative errors in the real and imaginary parts of the model fits in Figs. 12 and 13 can be found in the supplementary material (Section S7).

Log-likelihood analysis of diffusion timescales.—The fits of diffusion times to experimental data can be further probed by examining the underlying likelihood landscape in the $(\tau_{d,+}, \tau_{d,-})$ plane. As we did for synthetic data, we plot here the log-likelihoods in Fig. 16, minimising over $U_\pm^{(0)''}$. The DoDs chosen (50% and 60%) are ones at which the timescale estimates from EIS vs NLEIS differ

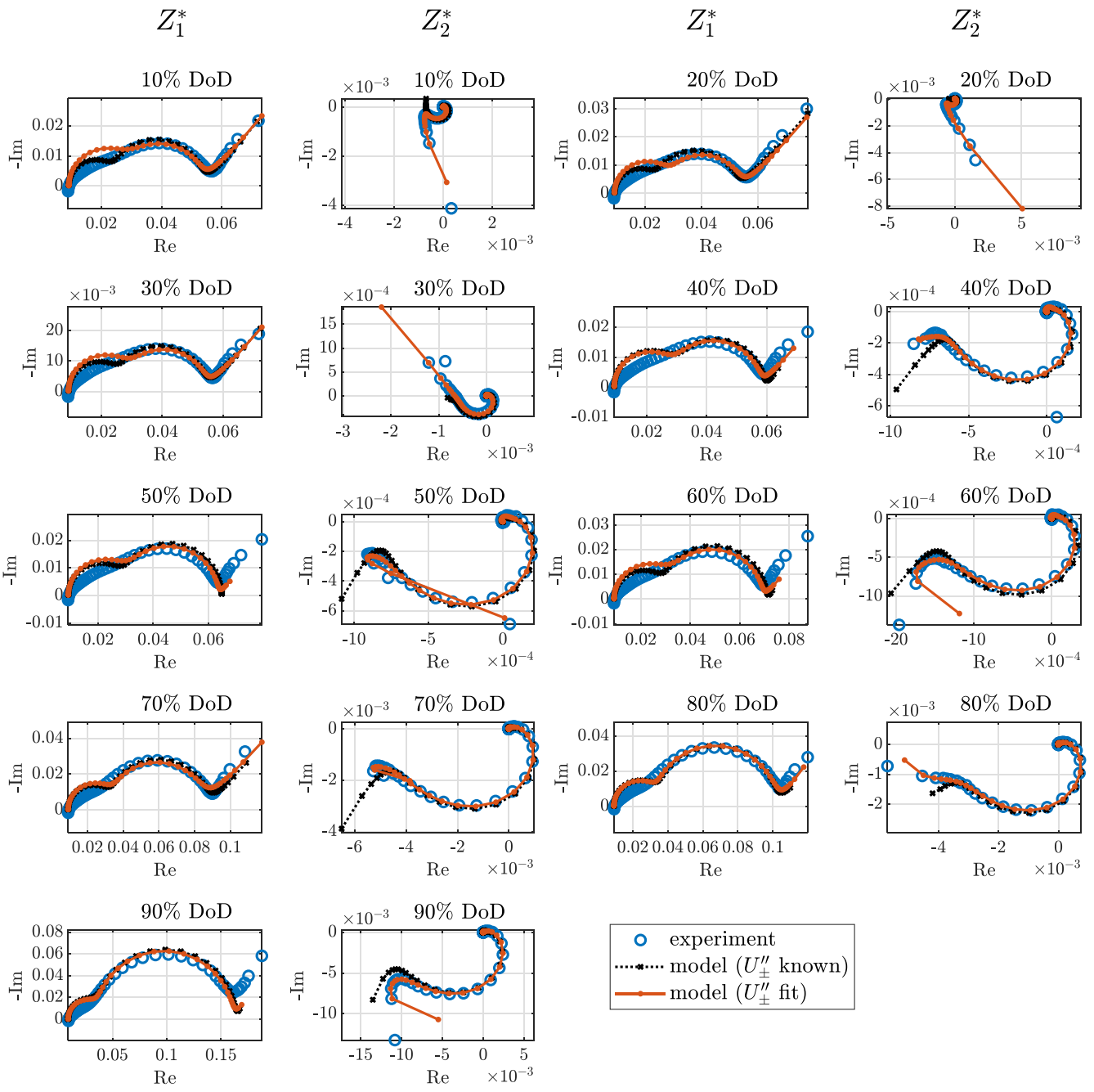

Figure 13. Simultaneous fits of the model impedances $Z_1^{(1)*}$ (fundamental) and $Z_2^{(2)*}$ (second harmonic) to corresponding experimental data. Z_1^*, Z_2^* units are in VA^{-1} (Ohms) and VA^{-2}. Two cases, where $U_\pm''$ is either fixed (assumed known) or chosen as a fitting parameter are shown. Fits performed at each DoD in the range 10%, 20%,… 90% separately, increasing from top left to the bottom right panel. Parameter estimates are given in Fig. 15.

significantly. The rest of the parameters are fixed at their estimated values from Fig. 15.

The l_1 landscape (Z_1^*) clearly shows unidentifiability given by the red line, i.e. 89. Here this is likely due to insufficient data at lower frequencies, as 89 also holds if only the high frequency approximation 48 is taken in the Warburg impedance. In the experiments, we were limited to a minimum allowable frequency of 0.01 Hz by the Kikusui PBZ60-6.7 power supply. This was not an issue when estimating from synthetic data (Fig. 11) as we were able to generate data at arbitrarily low frequencies—observe that the diffusion tail in Fig. 8i becomes close to vertical at the lowest frequencies. This unidentifiability valley was therefore not present, with one (or 2) local minima present instead.

The l_2 landscape (Z_2^*) in Fig. 16 has its minima considerably far from where l_1 predicts they should be. Further, the depth of l_2 minima overwhelms those in l_1 when combined in $l_{12} = l_1 + l_2$. This differs significantly from the behavior for synthetic data where the model exactly matches that used to generate the data, i.e. there is no model error, only approximation error due to the expansion in $\hat{I}$, and noise. In that case, the results showed that the fundamental is more dominant, with deeper minima in l_1 than l_2.

This inconsistency between the minima of l_1 and l_2 suggests that there may be deficiencies in the diffusion model even though the model is able to to fit the data very well. Here we considered a nonlinear diffusion model, but to alleviate these issues one may need to consider other approaches, e.g. those incorporating phase-field dynamics (such as Cahn—Hilliard) which have shown to better

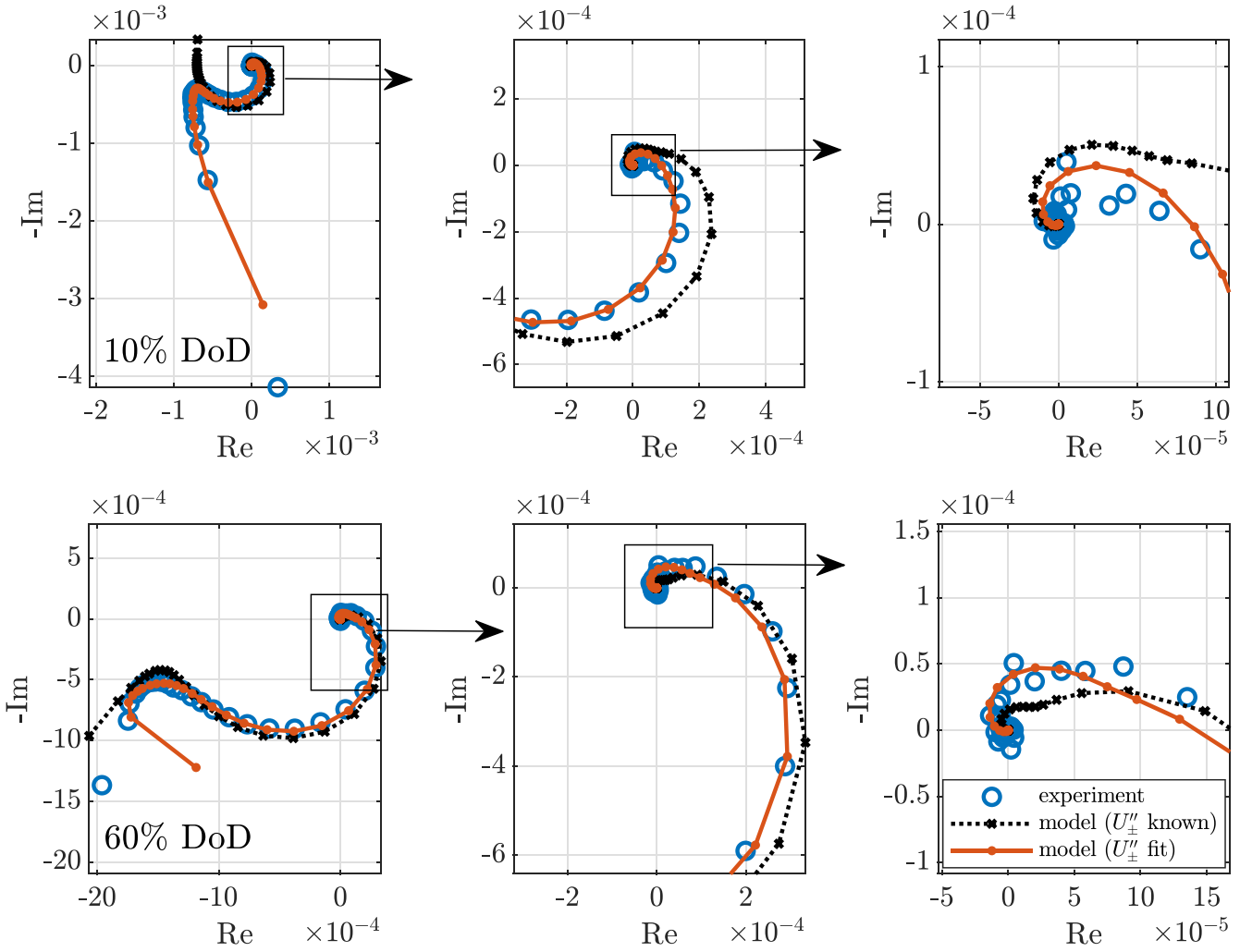

Figure 14. Successive zoom-ins on selected Z_2^* impedances in Fig. 13. The top row is at 10% DoD, and the bottom row is at 60% DoD.

represent lithiation in some electrode materials, e.g. graphite.[38] On the other hand, it may be that a single representative particle for each electrode is inadequate, or that large-scale geometric effects are important, or the inclusion of transport in the electrolyte is necessary. These results suggest NLEIS could be a promising tool for model selection. Other dynamics that may also relate to this inconsistency are those in the electrolyte, e.g. diffusion and migration of lithium, which have been neglected here.

Model validation in the time domain.—We have parameterized the nonlinear SPM using experimental NLEIS (frequency-domain) data and now proceed to validate the model performance and parameters by numerical solution in the time domain. We considered a current demand based on an electric vehicle drive cycle (see Ref. 39) with measurements taken on the same model of Kokam cell. Current was specified at 1 second intervals, with peaks reaching 4.4 A (or C-rates of 6), and initiated at 0% DoD. The model 15–24 was solved using this profile as an input, which was interpolated using piecewise-cubic Hermite interpolating polynomials (PCHIP) to ensure no overshooting of the data. Further details of numerical methods are given in the Methods.

We compared the model performance using two parameter sets: estimates from EIS data, and estimates from NLEIS data (see Fig. 15). We used NLEIS parameters for the case where $U''_\pm$ were considered unknown. For $\beta_\pm$, $C_\pm$, $\tau_{\mathrm{d},\pm}$, we chose single representative values by averaging over the full range of DoDs (with the average of $\tau_{\mathrm{d},\pm}$ taken on $\log \tau_{\mathrm{d},\pm}$). For $\chi_\pm$, we converted Fig. 15 data from DoD to stoichiometry $c_\pm$ and interpolated (PCHIP) to give the functions $\chi_+(c_+)$, $\chi_-(c_-)$.[b] The parameter values used are summarized in Table I.

Comparison between the model and experiment is shown in Fig. 17. In general, the model results with either parameter set (EIS or NLEIS) agree excellently with the measured data over the full duration (≈20 min), with no parameter tuning performed.[c] Even the EIS predictions show an RMSE of only 15.2 mV and no overall drift in error as time increases. This is a marked improvement over the linear SPM of Bizeray et al.[24] where, for the same cells and validation data, they required the linearized OCPs to be adjusted to correct for drift in the DoD . Our model exhibited no discernable drift and we considered a longer drive cycle simulation than Bizeray et al.[24] (≈17 mins vs 9 mins).

The predictions from NLEIS, however, agree even better with the measured voltage data, with a lower RMSE of 11.1 mV. We conclude that NLEIS can provide better estimates of the reaction kinetic parameters ($\chi_\pm$, $\beta_\pm$, and $C_\pm$). Looking at the stoichiometries on the surface of electrode particles (Fig. 17d) we see appreciable differences only in the negative electrode, but this has minimal effect on the voltage since $U_-(c_-)$ is mostly flat over the range of c_- operated in. Hence, diffusion timescale estimates from either method

[b] $\chi_\pm$ were originally assumed constant in the model, but making them depend on $c_\pm$ accounts for errors in the functional form of $R_\pm(c_\pm)$, 24.

[c] The series resistance R_s^* was changed before simulation to 20 mΩ (taken from Fig. 4 of Ref. 24)) since the drive cycle measurements were performed using a different test rig, but no subsequent changes to R_s^* were made.

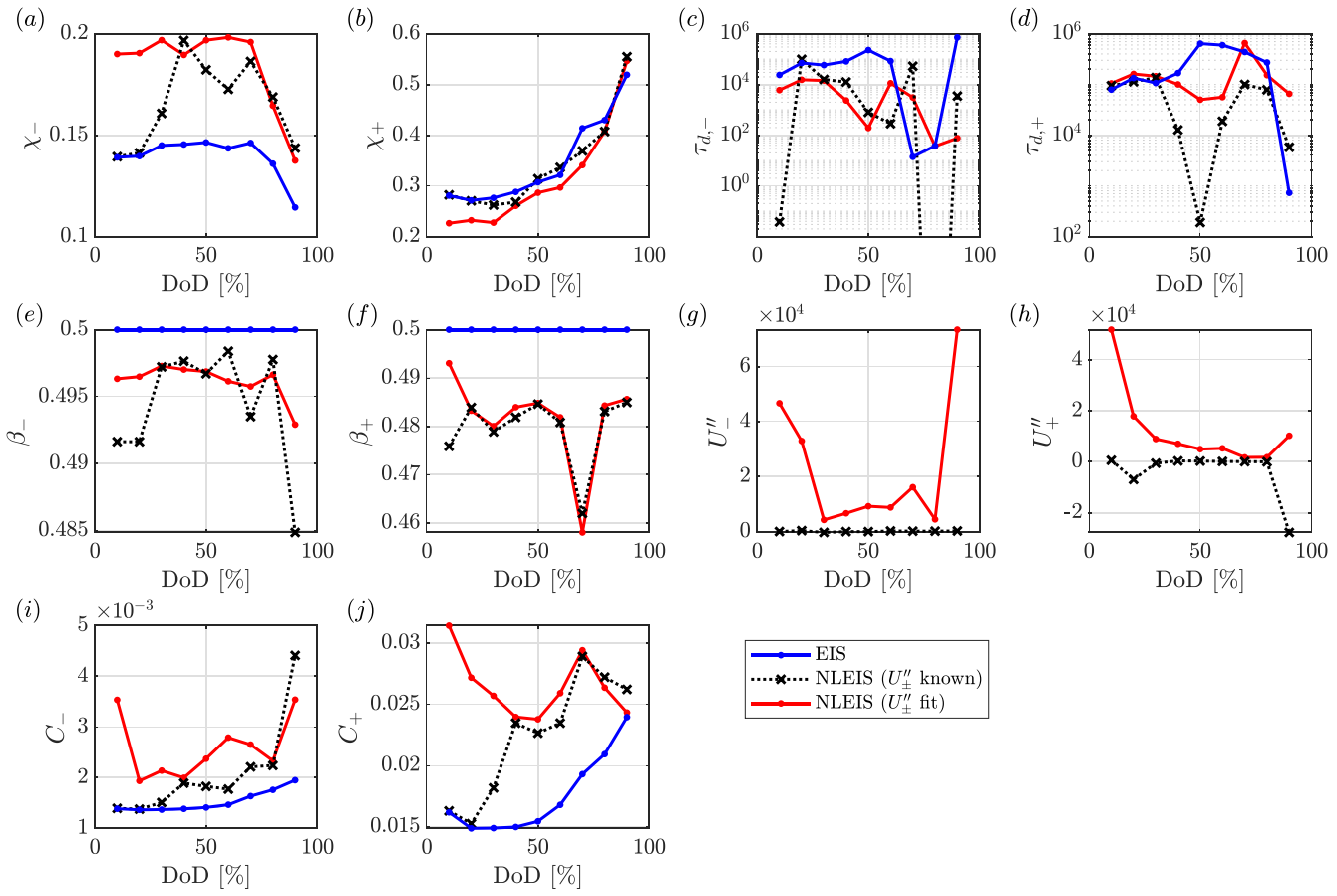

Figure 15. Parameter values from fitting to experimental EIS data (Z_1^* only) or NLEIS data (Z_1^* and Z_2^*) at different DoDs, from 10% to 90%. Kinetic parameters are in the left two columns (*a*, *b*, *e*, *f*, *i*, *j*), with diffusion timescales and OCP parameters in the remaining two; β_+ and β_- were taken as 0.5 in the EIS fits.

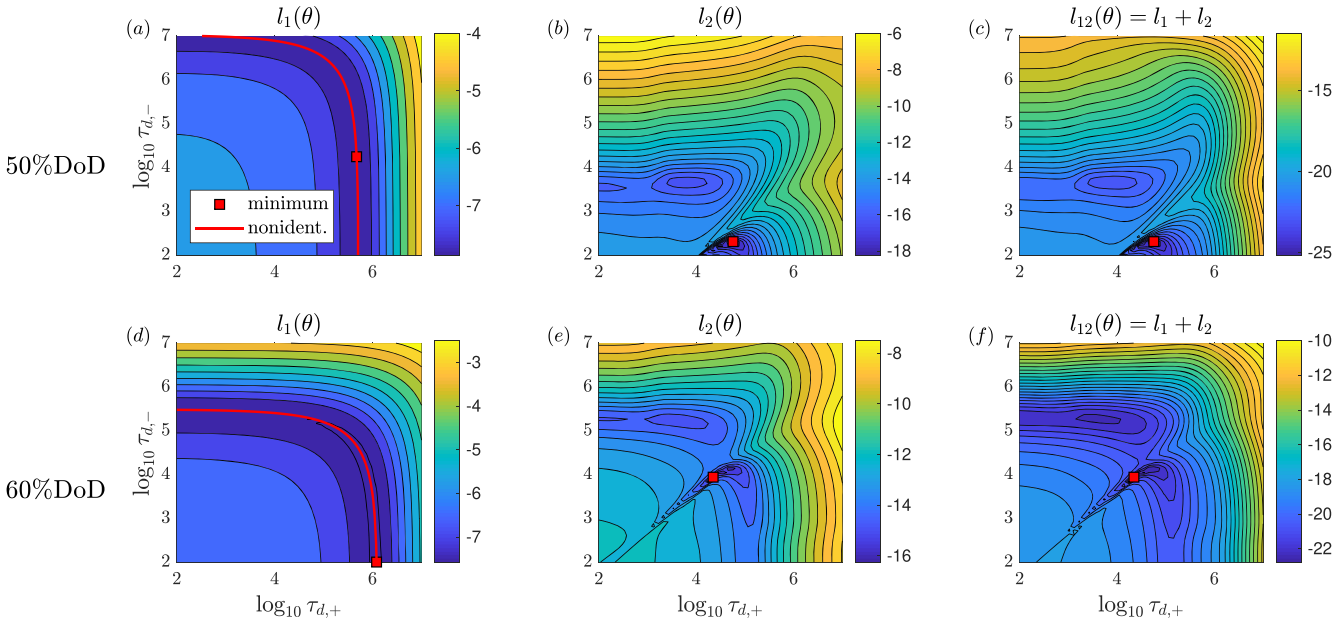

Figure 16. Log-likelihoods in the diffusion timescale plane $\tau_{d,+}$-$\tau_{d,-}$, using experimental data. Same as Fig. 10 but now at each point we have minimised over U''_- and U''_+.

are sufficient for good voltage accuracy in the time domain, but predictions of internal states may differ greatly, which will have consequences for degradation modelling.

Conclusions

In this paper, we presented a comprehensive study on the application of NLEIS to a standard physical model of a lithium-

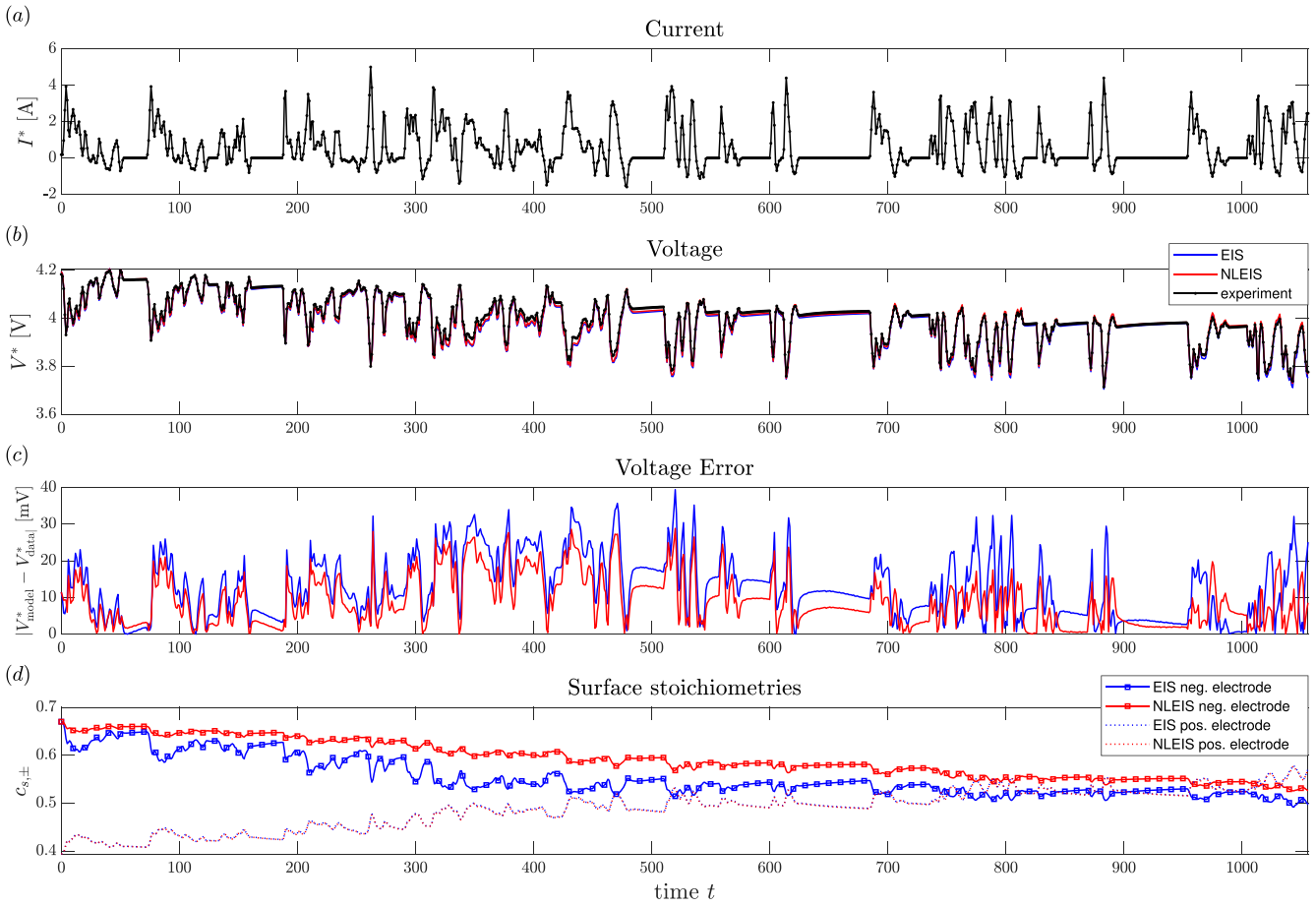

Figure 17. Model validation in the time domain, corresponding to a drive cycle of prescribed current (a). The terminal voltage from experiment[39] and two model simulations, using parameter values (Table I) from fitting to EIS or NLEIS data, are in (b). Also shown are (c) the absolute voltage error, and (d) surface stoichiometries $c_{s,\pm}$ in each electrode for each simulation.

ion battery: the single particle model. We derived a suite of analytical formulae for the fundamental harmonic and second harmonic impedances resulting from this model, and then interpreted each contribution to the formulae physically. Signatures of various processes and model nonlinearities were identified in the higher harmonics, in particular: (i) asymmetric charge transfer in Butler—Volmer kinetics; (ii) concentration dependence of the exchange current density; (iii) nonlinearity of the electrode OCPs; and (iv) nonlinearity of solid-state diffusion (i.e. concentration dependence of the diffusivity).

From our nonlinear impedance formulae, we explored how the second harmonic impedance in combination with the usual fundamental impedance can be used to improve parameter identifiability, both structurally and practically, over the use of the fundamental alone (EIS). Structurally, NLEIS can identify new parameters not possible from EIS, e.g. charge transfer coefficients (usually assumed to be 1/2 for Li-ion batteries), and improve the identifiability of the remaining parameters.

To investigate the impact of NLEIS on practical identifiability, we implemented maximum likelihood parameter estimation. First, we demonstrated the procedure using synthetic data and bootstrap resampling, showing that one can robustly determine all the model parameter groups (kinetic and diffusive) from NLEIS data. The second harmonic has a lower signal-to-noise ratio resulting in larger variances for some parameters, but these uncertainties are comparable in magnitude to model error, e.g. due to the small excitation amplitude approximation.

Finally, our parameter estimation procedure was applied to experimental NLEIS data that was collected from a commercial cell. We could fit the impedance data very well, capturing many of the key features of both harmonics. All the kinetic parameters were determined, and the charge transfer coefficients were found to deviate slightly from 1/2, albeit remaining within 10%. Validation of the model and its parameterization from either EIS or NLEIS data was conducted in the time domain with a drive cycle experiment, where an improvement in accuracy was observed for the NLEIS parameterization, showing that the technique is beneficial when the model is used in practice.

Areas of further work could consider the impacts of several physical mechanisms that were neglected here, such as transport through SEI layers and in the electrolyte. To keep a similar level of model complexity, one could consider the latter by extending the current analysis to the single particle model with electrolyte (SPMe).[29] The electrolyte introduces additional diffusive effects which may address the difficulties observed here with fitting the diffusion tails in a consistent manner. Other solid-state transport models, such as phase-field models,[38] could also be considered, and NLEIS used as a model selection tool. In addition, extending the minimum frequency measured experimentally could improve diffusion time estimates. Exploring the nonlinear frequency response of higher capacity cells, other lithium-ion battery chemistries, such as lithium-ion phosphate and lithium titanate, at different temperatures and as batteries age, would be interesting and valuable future work. Finally, metrics to quantify model parsimony could be considered, i.e. to analyze whether there are too many (or too few) parameters, and to compare different model structures.

Acknowledgments

This research was funded in whole, or in part, by the EPSRC Faraday Institution Multiscale Modelling project (EP/S003053/1, grant number FIRG025). The authors also wish to thank Robert Timms and Steven Psaltis for helpful discussions. For the purpose of Open Access, the authors have applied a CC BY public copyright licence to any Author Accepted Manuscript (AAM) version arising from this submission.

ORCID

Toby L. Kirk https://orcid.org/0000-0002-6700-0852
Adam Lewis-Douglas https://orcid.org/0000-0001-9451-0631
David Howey https://orcid.org/0000-0002-0620-3955

References

1. C. Iclodean, B. Varga, N. Burnete, D. Cimerdean, and B. Jurchiş, "Comparison of different battery types for electric vehicles." *IOP Conference Series: Materials Science and Engineering* **252**, 012058 (2017).
2. M. Doyle, T. M. Fuller, and J. Newman, "Modeling of galvanostatic charge and discharge of the lithium/polymer/insertion cell." *J. Electrochem. Soc.*, **140**, 1526 (1993).
3. Y. Barsukov and J. R. Macdonald, *Electrochemical Impedance Spectroscopy* (American Cancer Society) 1 (2012).
4. F. Ciucci, "Modeling electrochemical impedance spectroscopy." *Current Opinion in Electrochemistry*, **13**, 132 (2019), fundamental and Theoretical Electrochemistry: Physical and Nanoelectrochemistry.
5. M. D. Murbach and D. T. Schwartz, "Extending newman pseudo-two-dimensional lithium-ion battery impedance simulation approach to include the nonlinear harmonic response." *J. Electrochem. Soc.*, **164**, E3311 (2017).
6. N. Harting, N. Wolff, F. Röder, and U. Krewer, "Nonlinear frequency response analysis (nfra) of lithium-ion batteries." *Electrochimica Acta*, **248**, 133 (2017).
7. T. J. McDonald and S. Adler, "(invited) theory and application of nonlinear electrochemical impedance spectroscopy." *ECS Trans.*, **45**, 429 (2012).
8. J. Wilson, D. Schwartz, and S. Adler, "Nonlinear electrochemical impedance spectroscopy for solid oxide fuel cell cathode materials." *Electrochimica Acta*, **51**, 1389 (2006).
9. J. R. Wilson, M. Sase, T. Kawada, and S. B. Adler, "Measurement of oxygen exchange kinetics on thin-film $La_0.6Sr_0.4CoO_3$ using nonlinear electrochemical impedance spectroscopy." *Electrochem. Solid-State Lett.*, **10**, B81 (2007).
10. T. Kadyk, R. Hanke-Rauschenbach, and K. Sundmacher, "Nonlinear frequency response analysis of pem fuel cells for diagnosis of dehydration, flooding and co-poisoning." *J. Electroanalytical Chemistry*, **630**, 19 (2009).
11. T. Kadyk, R. Hanke-Rauschenbach, and K. Sundmacher, "Nonlinear frequency response analysis for the diagnosis of carbon monoxide poisoning in pem fuel cell anodes." *J. Appl. Electrochem.*, **41**, 1021 (2011).
12. N. Xu and J. Riley, "Nonlinear analysis of a classical system: the double-layer capacitor." *Electrochem. Commun.*, **13**, 1077 (2011).
13. N. Xu and D. J. Riley, "Nonlinear analysis of a classical system: the faradaic process." *Electrochimica Acta*, **94**, 206 (2013).
14. F. Fasmin and R. Srinivasan, "Review: nonlinear electrochemical impedance spectroscopy." *J. Electrochem. Soc.*, **164**, H443 (2017).
15. M. D. Murbach, V. W. Hu, and D. T. Schwartz, "Nonlinear electrochemical impedance spectroscopy of lithium-ion batteries: Experimental approach, analysis, and initial findings." *J. Electrochem. Soc.*, **165**, A2758 (2018).
16. N. Harting, N. Wolff, and U. Krewer, "Identification of lithium plating in lithium-ion batteries using nonlinear frequency response analysis (nfra)." *Electrochimica Acta*, **281**, 378 (2018).
17. N. Wolff, N. Harting, M. Heinrich, F. Röder, and U. Krewer, "Nonlinear frequency response analysis on lithium-ion batteries: a model-based assessment." *Electrochimica Acta*, **260**, 614 (2018).
18. N. Wolff, N. Harting, M. Heinrich, and U. Krewer, "Nonlinear frequency response analysis on lithium-ion batteries: process identification and differences between transient and steady-state behavior." *Electrochimica Acta*, **298**, 788 (2019).
19. C. Fan, K. O'Regan, L. Li, E. Kendrick, and W. Widanage, "Frequency domain non-linear characterization and analysis of lithium-ion battery electrodes." *J. Energy Storage*, **36**, 102371 (2021).
20. C. Fan, T. R. Grandjean, K. O'Regan, E. Kendrick, and W. D. Widanage, "Understanding non-linearity in electrochemical systems using multisine-based non-linear characterization." *Transactions of the Institute of Measurement and Control* (2021).
21. J. M. Reniers, G. Mulder, and D. A. Howey, "Review and performance comparison of mechanical-chemical degradation models for lithium-ion batteries." *J. Electrochem. Soc.*, **166**, A3189 (2019).
22. J. M. Reniers, G. Mulder, S. Ober-Blöbaum, and D. A. Howey, "Improving optimal control of grid-connected lithium-ion batteries through more accurate battery and degradation modelling." *J. Power Sources*, **379**, 91 (2018).
23. L. D. Couto, J. Schorsch, N. Job, A. Léonard, and M. Kinnaert, "State of health estimation for lithium ion batteries based on an equivalent-hydraulic model: an iron phosphate application." *J. Energy Storage*, **21**, 259 (2019).
24. A. M. Bizeray, J. Kim, S. R. Duncan, and D. A. Howey, "Identifiability and parameter estimation of the single particle lithium-ion battery model." *IEEE Transactions on Control Systems Technology*, **27**, 1862 (2019).
25. S. Atlung, K. West, and T. Jacobsen, "Dynamic aspects of solid solution cathodes for electrochemical power sources." *J. Electrochem. Soc.*, **126**, 1311 (1979).
26. G. Ning and B. N. Popov, "Cycle life modeling of lithium-ion batteries." *J. Electrochem. Soc.*, **151**, A1584 (2004).
27. J. S. Horner, G. Whang, D. S. Ashby, I. V. Kolesnichenko, T. N. Lambert, B. S. Dunn, A. A. Talin, and S. A. Roberts, "Electrochemical modeling of gitt measurements for improved solid-state diffusion coefficient evaluation." *ACS Appl. Energy Mater.*, **4**, 11460 (2021).
28. E. McTurk, C. R. Birkl, M. R. Roberts, D. A. Howey, and P. G. Bruce, "Minimally invasive insertion of reference electrodes into commercial lithium-ion pouch cells." *ECS Electrochem. Lett.*, **4**, A145 (2015).
29. S. G. Marquis, V. Sulzer, R. Timms, C. P. Please, and S. J. Chapman, "An asymptotic derivation of a single particle model with electrolyte." *J. Electrochem. Soc.*, **166**, A3693 (2019).
30. Kokam Cell SLPB533459H4 Data Sheet (Accessed 2022). https://www.custom-power.com/documents/SLPB533459H4.pdf.
31. R Bellman and K Åström, "On structural identifiability." *Mathematical Biosciences*, **7**, 329 (1970).
32. B. Efron and R. Tibshirani, *An Introduction to the Bootstrap* (London, Chapman and Hall/CRC) (1993).
33. D. Cox, *Principles of Statistical Inference* (Cambridge, Cambridge University Press) (2006).
34. M. J. Simpson, R. E. Baker, S. T. Vittadello, and O. J. Maclaren, "Practical parameter identifiability for spatio-temporal models of cell invasion." *Journal of The Royal Society Interface*, **17**, 20200055 (2020).
35. M. Ecker, S. Käbitz, I. Laresgoiti, and D. U. Sauer, "Parameterization of a physico-chemical model of a lithium-ion battery: II. Model validation." *J. Electrochem. Soc.*, **162**, A1849 (2015).
36. J. Schmalstieg, C. Rahe, M. Ecker, and D. U. Sauer, "Full cell parameterization of a high-power lithium-ion battery for a physico-chemical model: part I. physical and electrochemical parameters." *J. Electrochem. Soc.*, **165**, A3799 (2018).
37. C.-H. Chen, F. B. Planella, K. O'Regan, D. Gastol, W. D. Widanage, and E. Kendrick, "Development of experimental techniques for parameterization of multi-scale lithium-ion battery models." *J. Electrochem. Soc.*, **167**, 080534 (2020).
38. T. R. Ferguson and M. Z. Bazant, "Phase transformation dynamics in porous battery electrodes." *Electrochimica Acta*, **146**, 89 (2014).
39. S. Zhao, S. R. Duncan, and D. A. Howey, "Observability analysis and state estimation of lithium-ion batteries in the presence of sensor biases." *IEEE Transactions on Control Systems Technology*, **25**, 326 (2017).